**Abstract** An overview is presented of the current state-of-the-art in silicon nanophotonic ring resonators. Basic theory of ring resonators is discussed, and applied to the peculiarities of submicron silicon photonic wire waveguides: the small dimensions and tight bend radii, sensitivity to perturbations and the boundary conditions of the fabrication processes. Theory is compared to quantitative measurements. Finally, several of the more promising applications of silicon ring resonators are discussed: filters and optical delay lines, label-free biosensors, and active rings for efficient modulators and even light sources.
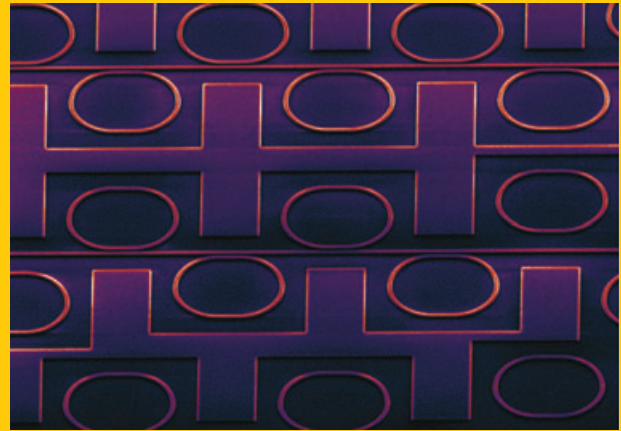
Silicon microring resonators

Wim Bogaerts[*]**, Peter De Heyn, Thomas Van Vaerenbergh, Katrien De Vos, Shankar Kumar Selvaraja, Tom Claes, Pieter Dumon, Peter Bienstman, Dries Van Thourhout, and Roel Baets**

1. Introduction

Silicon photonics has become one of the most promising photonic integration platforms in the last years. This can be mainly attributed to the combination of a very high index contrast and the availability of CMOS fabrication technology [1], which allows the use of electronics fabrication facilities to make photonic circuitry [1–5]. Passive silicon waveguide structures have shown an unprecedented reduction in footprint of waveguides, and especially wavelength-selective devices [6, 7]. Ring resonators are a prime example of this. In addition, over the past years there have been many demonstrations of integrated active devices including modulators [2, 8, 9], Germanium-based photodetectors and even III-V integrated sources and detectors [10–13].

Ring resonators play an important role in the success of silicon photonics, because silicon enables ring resonators of an unprecedented small size. A generic ring resonator consists of an optical waveguide which is looped back on itself, such that a resonance occurs when the optical path length of the resonator is exactly a whole number of wavelengths. Ring resonators therefore support multiple resonances, and the spacing between these resonances, the *free spectral range* (FSR), depends on the resonator length. As we will discuss in Sect. 4, for many applications it is preferred to have a relatively large FSR (several nm), and this implies the use of small rings. This translates into a very hard requirement for the optical waveguide: to make a compact ring, a small bend radius is required, and this in turn is only possible with high-contrast waveguides with strong confinement. Some examples of Silicon ring resonators are shown in Fig. 3.

Because of the very high refractive index contrast between silicon and its oxide (or air), single-mode strip waveguides (so-called photonic wires) can have bend radii below 5 μm. This allows for extremely compact rings, even with an FSR over 20 nm at telecom wavelengths around 1550 nm. This is in stark contrast with lower contrast material systems where rings need to be much larger.

A ring resonator as a stand-alone device only becomes useful when there is a coupling to the outside world. The most common coupling mechanism is using codirectional evanescent coupling between the ring and an adjacent bus waveguide. As will be discussed in more detail in the next section, the transmission spectrum of the bus waveguide with a single ring resonator will show dips around the ring resonances. This way, the ring resonator behaves as a spectral filter, which can be used for applications in optical communication, especially *wavelength division multiplexing* (WDM). Alternatively, these ring spectra can by used for sensing: as we will discuss in Sect. 2.5, the position and the shape of the resonance dips are very sensitive to a variety of effects, which can be detrimental (stability of a filter) or advantageous (as a sensor, or for tuning). We will discuss some applications in Sect. 4.

In this paper we will give an overview of the field of silicon microring resonators. We will start with a brief theoretical discussion of general ring resonator properties, and expand that to explore the parameters that might influence a silicon microring: this will indeed show that the use of high-contrast silicon comes with benefits, but also with significant drawbacks with respect to tolerances. To illustrate the various effects we show measurements in our own lab.
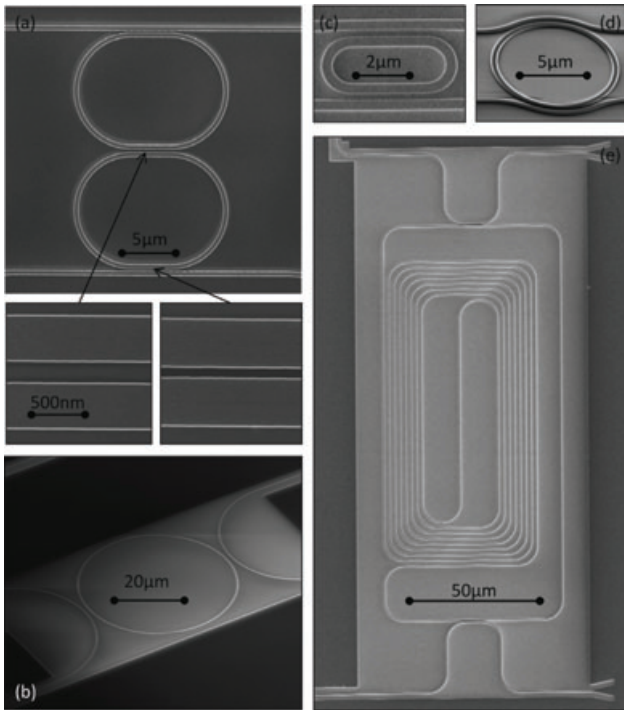
Photonics Research Group, Ghent University – imec, Department of Information Technology
[*] Corresponding author: e-mail: wim.bogaerts@intec.ugent.be

Figure 1 Examples of silicon ring resonators. (a) Double ring resonator with tuned directional coupling sections, (b) Circular ring with large coupler gaps, (c) Ultra-small racetrack ring with 1 μm bend radius, (d) ring with conformal coupling sections, (e) Large folded-spiral ring.

However, in many cases similar results were obtained by other groups. Finally, we discuss possible applications of ring resonators, with a focus on optical delay lines, biosensors and active rings.

2. Properties of a ring resonator

Before going into detail into the specifics of silicon microring resonators, we first discuss the generic properties of ring resonators. This will help us to further understand the unique possibilities, as well as the limitations of silicon microrings.

Optical microresonators are extensively described in literature [6, 14, 15]. In general a ring resonator consists of a looped optical waveguide and a coupling mechanism to access the loop. When the waves in the loop build up a round trip phase shift that equals an integer times 2π, the waves interfere constructively and the cavity is in resonance.

In what follows, we will briefly summarize all concepts and formulas that are needed to describe the functional behavior of ring resonators.

2.1. All-pass ring resonators

In its simplest form a ring resonator can be constructed by feeding one output of a directional coupler back into its input, the so-called all-pass filter (APF) or notch filter configuration (see Fig. 2A). The term *ring resonator* is typically used to indicate any looped resonator, but in the narrow sense it is a circular ring. When the shape is elongated with a straight section along one direction (typically along the coupling section) the term *racetrack resonator* is also used. We will use ring resonator throughout this paper, but most derivations and results apply to racetracks and loops of other shapes.

The basic spectral properties of an APF ring resonator can easily be derived by assuming continuous wave (CW) operation and matching fields. Under the assumption that reflections back into the bus waveguide are negligible (which is not necessarily the case in a silicon wire, see Sect. 2.6), we can write the ratio of the transmitted and incident field in the bus waveguide as [14]

$$\frac{E_{\text{pass}}}{E_{\text{input}}} = e^{i(\pi+\phi)} \frac{a - re^{-i\phi}}{1 - rae^{i\phi}} . \tag{1}$$

$\phi = \beta L$ is the single-pass phase shift, with L the round trip length and β the propagation constant of the circulating mode. a is the single-pass amplitude transmission, including both propagation loss in the ring and loss in the couplers. It relates to the power attenuation coefficient α [1/cm] as $a^2 = \exp(-\alpha L)$. By squaring Eq. (1), we obtain the intensity transmission T_{n} (we use subscript n from *notch* not to confuse with the pass transmission T_p from an add-drop filter in the next paragraph.):

$$T_{\text{n}} = \frac{I_{\text{pass}}}{I_{\text{input}}} = \frac{a^2 - 2ra\cos\phi + r^2}{1 - 2ar\cos\phi + (ra)^2} . \tag{2}$$

r is the self-coupling coefficient. Similarly, we can define k as the cross-coupling coefficients, and so r^2 and k^2 are the power splitting ratios of the coupler, and they are assumed to satisfy $r^2 + k^2 = 1$, which means there are no losses in the coupling section. This assumption can introduce a small error on the transmission power levels. The width of the resonance remains correct, as long as the losses that are
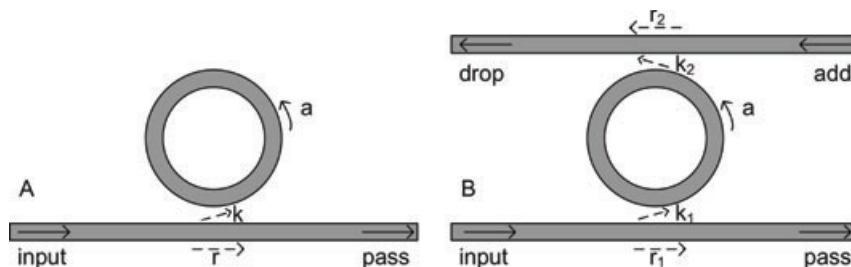

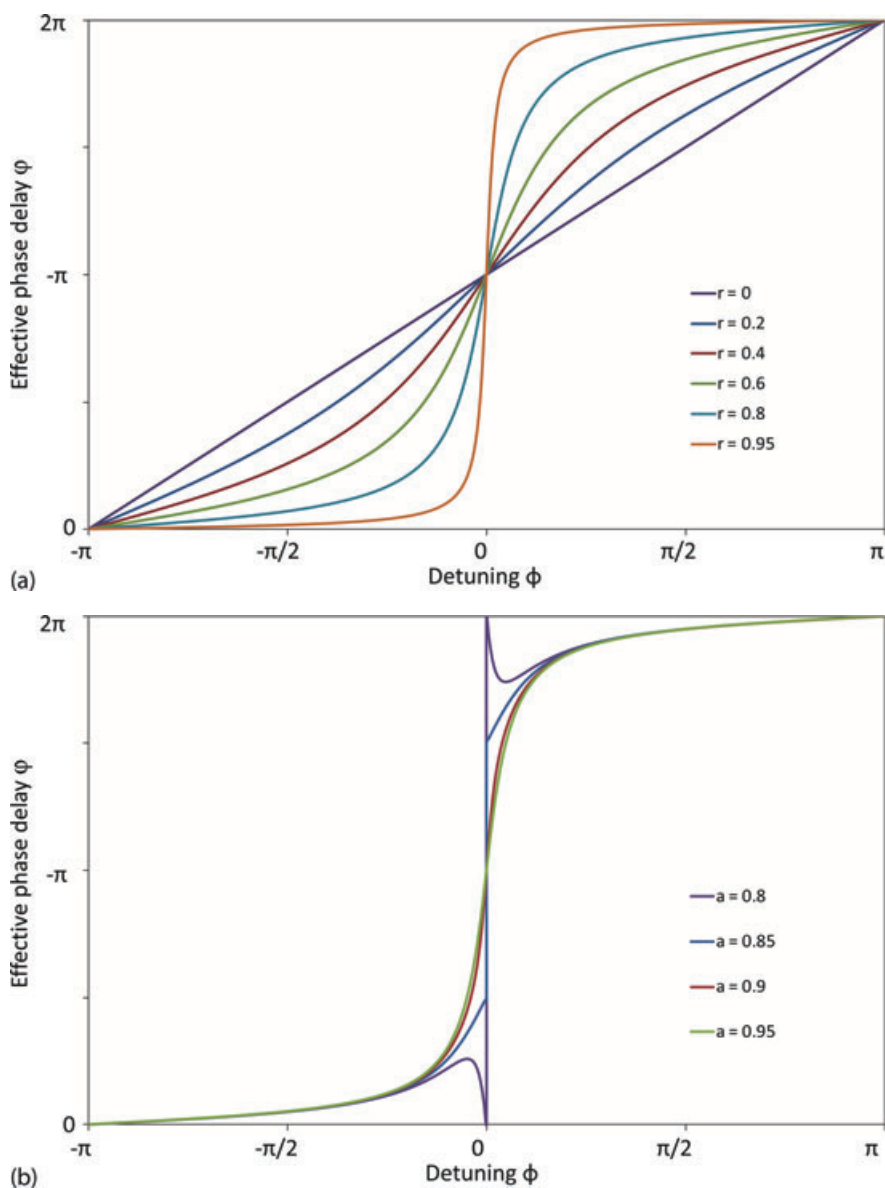**Figure 2** (A) All-pass and (B) add-drop ring resonator.

Figure 3 (online color at: www.lpr-journal.org) Effective phase delay of an all-pass filter with (a) $a = 1$ and various values of the self-coupling r, and (b) for $r = 0.85$ and different values of a. Note that for critical coupling $r = a = 0.85$ we get an abrupt π phase shift. For over and undercoupling, the phase shift is continuous, but in opposite direction [16].

introduced by the couplers are included in the resonator round trip loss coefficient a.

We find the ring to be on resonance when the phase ϕ is a multiple of 2π, or when the wavelength of the light fits a whole number of times inside the optical length of the ring:

$$\lambda_{\text{res}} = \frac{n_{\text{eff}}L}{m}, \qquad m = 1, 2, 3 \ldots . \qquad (3)$$

For ideal cavities with zero attenuation, $a \approx 1$, the transmission is unity for all values of detuning ϕ. Under critical coupling, when the coupled power is equal to the power loss in the ring $1 - a^2 = k^2$ or $r = a$, the transmission at resonance drops to zero. The phase argument of the field transmission varies periodically with frequency. All-pass resonators delay incoming signals via the temporary storage of optical energy within the resonator.

From Eq. (1) we can also calculate the effective phase shift φ induced by the ring resonator:

$$\varphi = \pi + \phi + \arctan \frac{r \sin \phi}{a - r \cos \phi} + \arctan \frac{ra \sin \phi}{1 - ra \cos \phi}. \quad (4)$$

The phase response for a ring with no intrinsic losses ($a = 1$) is plotted in Fig. 3 for different values of the self-coupling coefficient r. We see that for strong self-coupling (good resonances) the phase response becomes very steep near the resonance. A ring resonator can thus add a significant wavelength dependent phase shift, which, as we will discuss in Sect. 4.2, can be used to slow down light in an optical buffer. In the bottom part of Fig. 3 we see the phase response for different values of a (intrinsic ring loss) and a fixed $r = 0.85$. We see that for $r = a$ (critical coupling), the transmission experiences an abrupt π phase shift at the resonance wavelength. However, for $r < a$ (overcoupling), the transmission experiences continuous positive phase de-

lay, while for $r > a$ (undercoupling) the phase shift near the resonance shows a strong decrease, which is plotted as a 2π phase shift in Fig. 3b [16].

2.2. Add-drop ring resonators

When the ring resonator is coupled to two waveguides, the incident field is partly transmitted to the drop port (see Fig. 2B). The transmission to the pass and the drop port can also be derived from CW operation and matching the fields.

$$T_p = \frac{I_{\text{pass}}}{I_{\text{input}}} = \frac{r_2^2 a^2 - 2r_1 r_2 a \cos\phi + r_1^2}{1 - 2r_1 r_2 a \cos\phi + (r_1 r_2 a)^2}, \tag{5}$$

$$T_d = \frac{I_{\text{drop}}}{I_{\text{input}}} = \frac{(1 - r_1^2)(1 - r_2^2)a}{1 - 2r_1 r_2 a \cos\phi + (r_1 r_2 a)^2}. \tag{6}$$

If the attenuation is negligible ($a \approx 1$), critical coupling occurs at symmetric coupling ($k_1 = k_2$). For a lossy resonator, critical coupling occurs when the losses match the coupling as $r_2 a = r_1$.

2.3. Spectral characteristics

The characteristic parameters are indicated in Fig. 4. They depend on the losses and coupling coefficients and can be extracted directly from the formulas for transmission (2), (5), and (6). The results are listed below. In Sect. 3.3 we will perform the reverse operation: starting from the measured spectral characteristics, the losses and coupling coefficients of SOI ring resonators will be determined.

From expressions (2), (5), and (6) we can derive the full width at half maximum (FWHM) of the resonance spectrum for an all-pass ring resonator:

$$\text{FWHM} = \frac{(1 - ra)\lambda_{\text{res}}^2}{\pi n_g L \sqrt{ra}}, \tag{7}$$

and for an add-drop ring resonator configuration:

$$\text{FWHM} = \frac{(1 - r_1 r_2 a)\lambda_{\text{res}}^2}{\pi n_g L \sqrt{r_1 r_2 a}}. \tag{8}$$

Within a first order approximation of the dispersion, the wavelength range between two resonances or free spectral range (FSR) in function of wavelength equals:

$$\text{FSR} = \frac{\lambda^2}{n_g L} \tag{9}$$

with L the round trip length. The strong confinement in SOI wires allows for very sharp bends (radius down to 3 μm) with still low radiation. This largely increases the potential FSR of SOI ring resonators as compared to conventional optical resonators.

Note that in both FWHM and FSR we find the group index in the denominator, not the effective index n_{eff}. The group index takes into account the dispersion of the waveguide and is defined by

$$n_g = n_{\text{eff}} - \lambda_0 \frac{dn_{\text{eff}}}{d\lambda}. \tag{10}$$

The group index, and the corresponding group velocity $v_g = \frac{c}{n_g}$, describes the velocity at which the envelope of a propagating pulse travels and is a characteristic of a dispersive medium (or waveguide).

The on-off extinction ratio of the through port transmission is equal to $\frac{T_t}{R_{\text{min}}}$. For an APF ring configuration, we get for T_t and R_{min}:

$$T_t = \frac{(r + a)^2}{(1 + ra)^2}, \tag{11}$$

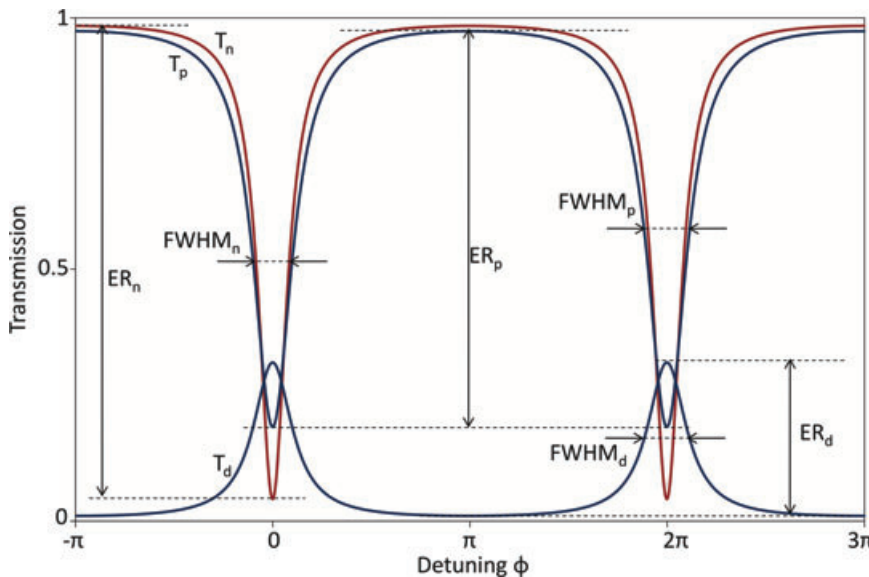$$R_{\text{min}} = \frac{(r - a)^2}{(1 - ra)^2}. \tag{12}$$

Figure 4   (online color at: www.lpr-journal.org) Transmission spectrum of an all-pass ring and the two outputs of add-drop ring with the important spectral features indicated. $a = 0.85$, $r = r_1 = r_2 = 0.9$. Because of the additional losses introduced by the second coupling section, the add-drop rings has a broader peak. Also, coupling is further from critical coupling, resulting in a smaller extinction ratio.

For an add-drop configuration, we can define the same ER $\frac{T_{max}}{T_d}$ for the drop transmission. At resonance, the ER between through and drop port of an add-drop resonator is given by $\frac{T_{max}}{R_{min}}$. T_t, R_{min}, T_{max} and T_d are defined as:

$$T_t = \frac{(r_2 a + r_1)^2}{(1 + r_1 r_2 a)^2}, \tag{13}$$

$$R_{min} = \frac{r_2^2 a^2 - 2 r_1 r_2 a + r_1^2}{(1 - r_1 r_2 a)^2}, \tag{14}$$

$$T_{max} = \frac{(1 - r_1^2)(1 - r_2^2) a}{(1 - r_1 r_2 a)^2}, \tag{15}$$

$$T_d = \frac{(1 - r_1^2)(1 - r_2^2) a}{(1 + r_1 r_2 a)^2}. \tag{16}$$

The finesse is defined as the ratio of FSR and resonance width,

$$\text{Finesse} = \frac{\text{FSR}}{\text{FWHM}}. \tag{17}$$

It is thus a measure of the sharpness of resonances relative to their spacing. The quality factor (Q-factor) is a measure of the sharpness of the resonance relative to its central frequency,

$$\text{Q-factor} = \frac{\lambda_{res}}{\text{FWHM}}. \tag{18}$$

The physical meaning of the finesse and Q-factor relates to the number of round-trips made by the energy in the resonator before being lost to internal loss and the bus waveguides. This is a temporal phenomenon and must be examined with the transient response. The mathematics are described in numerous text books and publications [14, 17, 18]. The finesse is found to represent within a factor of 2π the number of round-trips made by light in the ring before its energy is reduced to $1/e$ of its initial value. The Q-factor represents the number of oscillations of the field before the circulating energy is depleted to $1/e$ of the initial energy. To define the Q-factor, the microring is excited to a certain level and the rate of power decay is considered. From this point of view it is understood that round trip losses as well as coupling in the directional couplers are loss factors that need to be reduced to obtain high-Q resonances. Therefore an all-pass resonator will exhibit a higher Q-factor than an add-drop resonator (when both devices operate close to critical coupling).

We make a distinction between *loaded* Q and *unloaded* Q. The unloaded Q of a resonator is the Q-factor when the resonator would not be coupled to waveguides. When coupling to a waveguide, additional losses are introduced to the cavity. Hence, the loaded Q is always smaller than the unloaded Q. We always mean *loaded* Q when referring to Q-factor, unless it is specifically mentioned otherwise.

2.4. Losses and coupling

As we will discuss in more detail when covering silicon rings, we can separate the losses into different contributions:

waveguide propagation losses and losses in the coupling section. When we discuss a racetrack resonator, instead of a ring, we can add excess bend losses due to mismatch losses at the straight-bend transition. Losses in the coupling section originate from propagation losses, from additional sidewall roughness affecting the distributed intensity, and even from a mismatch in waveguide width caused by the fabrication process (see Sect. 3.1).

The roundtrip loss A includes the three loss contributors summarized above:

$$A[dB] = A'_{\text{propagation}} L + 2 A_{\text{coupler}} + 4 A_{\text{bend}}, \tag{19}$$

with $A'_{\text{propagation}}$ the propagation loss per unit of length, typically expressed in [dB/cm]. From Eq. (18) and (17) the Q-factor and finesse can be rewritten as a function of the physical parameters of an all-pass ring resonator:

$$\text{Q-factor} = \frac{\pi n_g L \sqrt{ra}}{\lambda_{res}(1 - ra)}, \tag{20}$$

$$\text{Finesse} = \frac{\pi \sqrt{ra}}{1 - ra}, \tag{21}$$

and for an add-drop ring resonator:

$$\text{Q-factor} = \frac{\pi n_g L \sqrt{r_1 r_2 a}}{\lambda_{res}(1 - r_1 r_2 a)}, \tag{22}$$

$$\text{Finesse} = \frac{\pi \sqrt{r_1 r_2 a}}{1 - r_1 r_2 a}. \tag{23}$$

In order to increase the Q-factor, it is crucial to reduce the losses in the cavity. Propagation losses are diminished by high quality SOI material and high quality processing [19]. Bend losses might be reduced by design of adiabatic bends that curve smoothly instead of circular bends [20].

The formula for Q-factor suggests that a better Q is obtained for large L and small cavity loss, but these two terms are not independent since the accumulated propagation loss increases with the cavity length. Figures 5 and 6 present theoretical calculations of the variation of Q-factor and finesse as a function of cavity length for different propagation losses and for add-drop and APF configurations. In these graphs, an initial loss factor due to bends (0.04 dB) and couplers (0.035 dB for an APF and 0.07 for an add-drop ring), based on realistic values measured on silicon ring resonators. The resonators operate at critical coupling, $r = a$ in the all-pass configuration, $r_1 = r_2 a$ in the add-drop configuration. r_2 was set to 0.99.

With propagation losses set to 2.7 dB/cm (corresponding to waveguide losses in a silicon wire with air cladding in the *imec* fabrication process [1]), the highest Q-factor that can be obtained under the given conditions is about $1.42 \cdot 10^5$ with an APF resonator of approximately 10 mm roundtrip length. The highest Q-factor for an add-drop resonator would be $1.36 \cdot 10^5$ for almost 13 mm in length. However, a larger length also leads to a lower finesse.
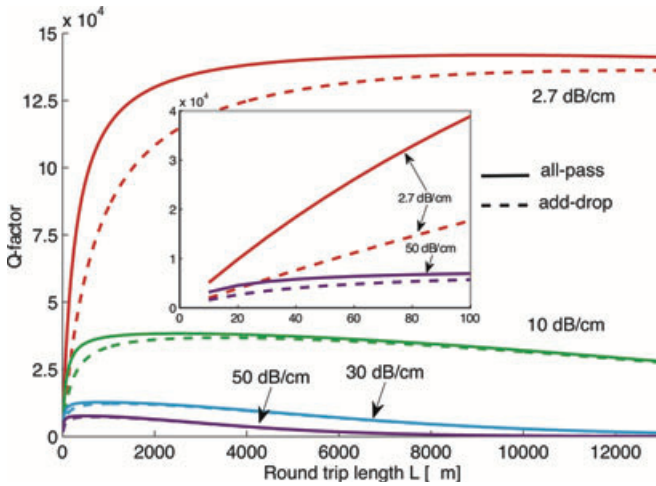
Figure 5 (online color at: www.lpr-journal.org) Quality factor as a function of cavity length for four propagation loss figures.
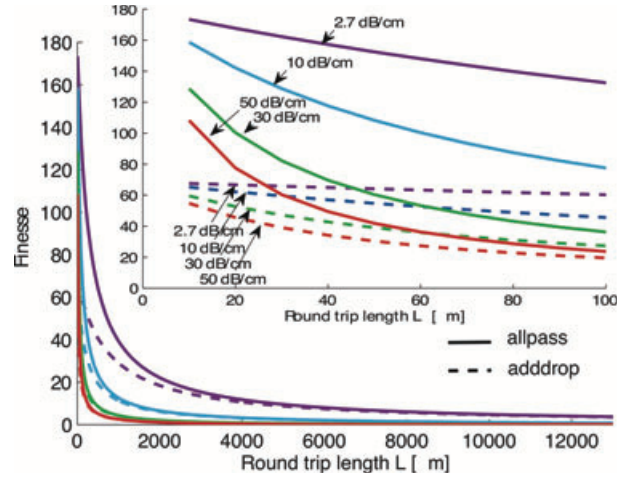

Figure 6 (online color at: www.lpr-journal.org) Finesse as a function of cavity length for four propagation loss figures.

2.5. Sensitivity

The resonance of the ring resonator depends on the optical roundtrip length of the ring, and the losses accumulated (all loss mechanisms combined, including coupling to bus waveguides). Therefore, ring resonators will be sensitive to a multitude of effects. that is why they are also attractive for use in sensing applications (see Sect. 4.3). We define sensitivity as the amount of wavelength shift $\Delta\lambda_{res}$ caused by a certain amount of whatever effect we are studying, be it temperature, physical deformation or compositional changes of the waveguide core or cladding. A shift of the resonance wavelength λ_{res} is essentially caused by a change of the effective index of the resonant mode n_{eff}. Based on Eq. (3), we get

$$\Delta\lambda_{res} = \frac{\Delta n_{eff} L}{m}, m = 1, 2, 3\ldots \qquad (24)$$

where m is the order of the resonant mode. n_{eff} is influenced by the refractive index of the cladding, which is altered upon sensing. As we will see in the next section, in submicron silicon waveguides, the waveguide dispersion can not be neglected. A change of n_{eff} will primarily alter λ_{res}, which in turn will influence n_{eff} due to the non-zero slope of $\frac{\partial n_{eff}}{\partial\lambda}$. In a first order approximation both effects can be decoupled:

$$\Delta\lambda_{res} = \frac{\left[\left(\frac{\partial n_{eff}}{\partial n_{env}}\right)_{\lambda_{res},n_{env}^0}\Delta n_{env} + \left(\frac{\partial n_{eff}}{\partial\lambda}\right)_{\lambda_{res},n_{env}^0}\Delta\lambda_{res}\right]\cdot L}{m}$$

With n_{eff}^0 at the initial resonance wavelength. After substitution in formulas (3) and (10) at $\lambda = \lambda_{res}$, a compact formula for the resonance wavelength shift with first order dispersion will appear:

$$\Delta\lambda_{res} = \frac{\Delta_{env} n_{eff} \cdot \lambda_{res}}{n_g} \qquad (25)$$

where $\Delta_{env} n_{eff}$ is the effective index shift caused by an environmental change, $\Delta_{env} n_{eff} = \left(\frac{\partial n_{eff}}{\partial n_{env}}\right)_{\lambda_{res},n_{env}^0}\Delta n_{env}$.

From the variational theorem of waveguides, $\Delta_{env} n_{eff}$ caused by a local change of dielectric constant $\Delta\varepsilon(x,y)$, can be expressed as [21–23]

$$\Delta_{env} n_{eff} = c\int\Delta\varepsilon\mathbf{E}_\nu\cdot\mathbf{E}_\nu^* dxdy \qquad (26)$$

where $\mathbf{E}_\nu(x,y)$ is the normalized modal electric field vector of the waveguide mode in the ring.

The ring response scales with the squared amplitude of the electric field at the perturbation and, therefore, with the fraction of the total modal power contained in the surface volume where the dielectric constant is modified. This fraction can be increased by changing the waveguide core dimension, and thus changing the confinement in any part of the core or cladding. A rigorous derivation of the sensitivity of n_{eff} of slab waveguides for variations of the environment was performed by Tiefenthaler et al. in [22].

2.6. Counterdirectional coupling

Each mode of a microring resonator can travel in two directions, the forward propagating mode, which is intentionally excited by the bus waveguide, and the backward propagating mode. Counterdirectional (or contra-directional) coupling is the mutual coupling between these two modes. When there is coupling, this will result in a net power transfer from the forward (deliberately excited) mode to the backward propagating mode, and this coupling also causes distortion to the ideal Lorentzian-shaped spectrum by resonance-splitting. To understand resonance-splitting due to counterdirectional coupling, we describe this system in temporal coupled-mode theory (TCMT) [18, 24, 25].

Consider an ideal resonator (e. g. circular symmetric, with perfect sidewall smoothness and without a coupling section), where the forward and backward traveling-wave modes are uncoupled, frequency-degenerate eigenmodes of the system. However, in practice, small perturbation which

can be felt by the optical mode can break this symmetry and couple the two traveling-wave modes. The traveling waves are then no longer uncoupled. However, the system will have two new eigenmodes (linear combinations of the original travelling-wave eigenmodes) which are uncoupled. In the case of a single point-like perturbation in the ring, such as the coupling section, the new eigenmodes are pure standing-wave modes, symmetric (a_+) and antisymmetric (a_-) w. r. to the perturbation [18]. Forward propagating light in the waveguide will then excite the symmetric and antisymmetric mode 90° out of phase. Due to symmetry breaking, these uncoupled eigenmodes are no longer degenerate, resulting in a resonance frequency shift and thus the spectrum will show resonance-splitting.

In principle, this perturbation could be induced by the presence of a bus waveguide [24], since the two standing waves will feel a slightly different environment (effective refractive index) causing the supermodes to resonate on a slightly different frequency. From the traveling-wave viewpoint, the directional coupler is then a periodically phase-matched scatterer into the backward propagation direction, thus building up the power in the counterpropagating mode and splitting the supermodes. A good introduction about the modelling of the back-reflection caused by the coupling section can be found in [26]. Also sidewall-roughness-induced backscattering has been predicted [27] and demonstrated [25, 28] to lead to deleterious resonance splitting.

As we will see in Sect. 3, in silicon waveguides the impact of the bus waveguide will rather be small in comparison with the impact of sidewall corrugation, such that the former effect can be ignored. However, in higher-order filters, with several coupling sections, it might limit designers to obtain a good extinction ratio. A solution has been proposed in [24] by choosing for a longer and weaker directional coupler that covers several propagation wavelengths of the ring mode, thus reducing the difference in environment between the modes.

Little et al. show in [27] that if the time to deplete the ring due to counterdirectional coupling becomes smaller than the time to charge up the ring to its steady-state value, resonance-splitting becomes visible in the spectrum of the resonator. This behavior is usually translated into $R > k^2$ with R the mutual coupling between the forward and backward propagation mode and k the external coupling. Because it is often desirable to keep k low to achieve a narrow line width, even minor reflections will cause problems in high-Q devices.

Next to resonance-splitting, counterdirectional coupling also causes power reflecting back into the input waveguide and/or the add-port. These reflections are usually referred to as surface-roughness induced backreflection which is common present in any high-index-contrast waveguide design and can accurately be quantified by inverse Fourier transforming the spectrum [29]. This backreflection is strongly enhanced by the resonances of the ring and increases with the groups index of the ring [30].

Even for a single given ring, the resonance splitting can strongly vary between different resonance wavelengths [31]. Following the arguments in [27], the depth of the sidewall

corrugation is mostly considered as a stochastic variable, corresponding with a gaussian correlation function with a fixed variance and correlation length. Both the variance and correlation length are determined by the fabrication process. The randomness of the roughness induces the unpredictability of the backscattering level at the different resonance wavelengths.

Recently it was experimentally demonstrated that backscattering is indeed a wavelength dependent random process whose statistics is independent of the shape, size, refractive index contrast, and technology of the waveguide [32]. However, it has been reported [33] that when resonators are fabricated with electron beam lithography, the surface-roughness can be semi-periodic, as it could consist of a group of ridges which have similar amplitude and period. In such case the roughness is better modeled as a quasi-grating. This reduces the unpredictability of the backscattering at a certain wavelength, as the backscattering level now becomes a determenistic function of the wavelength. It is expected that controlling the shape of the quasi-gratings in the fabricaion process enables to design microrings with predefined backscattering levels in a given wavelength range. Predicting the amount and occurrence of resonance-splitting enables new possibilities of applications such as fast light [34] and dense wavelength conversion [35].

3. Ring resonators in silicon

We will now apply the concepts in the previous section to silicon nanophotonic waveguides. First, we will discuss the peculiarities of silicon wires, and what makes them different from traditional waveguides. We will also discuss the directional coupler section. Then we will explore silicon ring resonators in detail, their sensitivities, but also their tuning potential and nonlinear properties.

3.1. Silicon waveguides

SOI waveguides channel light through transverse and lateral confinement in a silicon core (n=3.47) surrounded by a silicon oxide bottom cladding (n=1.44) and a low index top cladding (oxide or air). In most cases, silicon waveguides are fabricated using e-beam or optical lithography and reactive ion etching, often on CMOS manufacturing tools [1, 19, 36, 37].

To comply with a single-mode condition (for one polarization, at 1.55 μm wavelength) the cross section dimensions should be submicrometer in size, with typically increasing widths for decreasing thicknesses. Cross sections vary from a wide, thin 600×100 nm [38] to a square 300×300 nm [39]. The most commonly used dimensions are between 400 nm and 500 nm in width, and between 200 nm and 250 nm in height [1, 6, 37, 40]. The index contrast between core and cladding is very high, this gives rise to very strong confinement which enables light guiding in bends with very small radii without radiation losses.
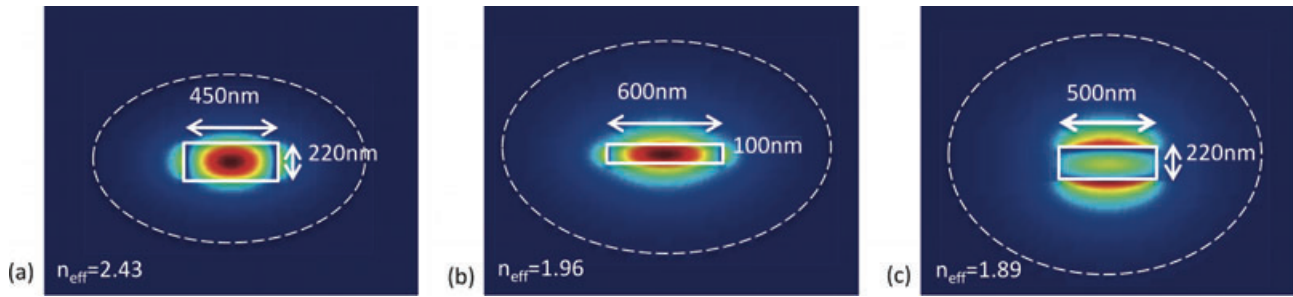
Figure 7 (online color at: www.lpr-journal.org)   Illustration of the mode spreading in three SOI waveguide cross sections (core $n_{Si} = 3.48$, cladding $n_{SiO_2} = 1.54$). (a) standard waveguide for TE polarized light (b) reduced interaction with vertical sidewalls and lower confinement, waveguide cross section used in [38] for the TE polarization (c) using TM-polarized light, no discontinuity at vertical sidewalls and lower confinement, waveguide cross sections used in [31].

At the core/cladding interface, the normal component of displacement $D = \varepsilon E$ must be continuous. Therefore the field amplitude at the cladding side of the interface will be stronger for a mode with the dominant E-field polarized normal to the interface. If the waveguide width is larger than its height (the most commonly used geometry), the ground mode will have a quasi TE polarization, with a strong discontinuity on the sidewall surface. Likewise, the TM mode will have a discontinuity on the top and bottom surface. Figure 7 illustrates the mode profiles for a waveguide with 450 nm width and 220 nm height.

Propagation losses in silicon wires originate from multiple sources, and recent advances in process technology (in various groups) have brought the losses down to 2–3dB/cm [19, 37, 41] with air cladding and less than 2dB/cm with oxide cladding [20, 41]. This difference can be explained by looking at different loss contributions.

Light scattering at sidewall roughness is considered to be the strongest effect [42, 43]. Due to the nature of the lithography fabrication process, roughness on the vertical sidewalls of the waveguide is unavoidable. This is visible in Fig. 8. A lot of effort is put into the optimization of fabrication processes to minimize the surface-roughness. The losses are correlated with the periodicity of the roughness as well as its dimensions, and scale dramatically with the index contrast [44–46]. The sidewalls are expected to exhibit a larger roughness as the typical fabrication process involves a dry etch process. Scattering at top surface roughness is much less severe: the RMS roughness induced by the polishing process is much smaller at about 0.1 nm [42–44].

Besides minimizing the surface-roughness by fabrication optimization, theoretical approaches based on three-dimensional analysis have been developed to adjust the cross section for a certain polarization to minimize the scattering and backscattering efficiency [47, 48]. However, one might be limited in designing the cross section by other effects such as polarization rotation and coupling to higher order modes, both resulting in an increased loss. A surface-roughness optimized waveguide cross section for TE-polarized light is presented in [38] for TE-polarized light. With a height of only 100 nm and a width of 600 nm, this cross section is still single mode and has 7× less scattering loss than a standard design of width 220 nm and
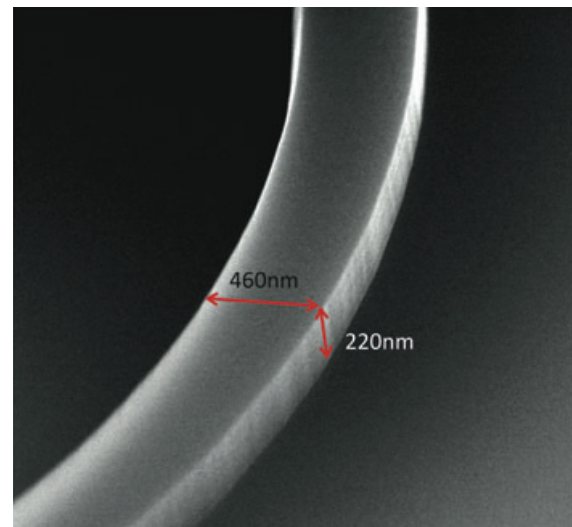

Figure 8 (online color at: www.lpr-journal.org)   Bird's eye SEM view of a photonic wire waveguides fabricated with the process from [19]. The sidewall roughness is clearly visible.

height 450 nm. This improvement is estimated based on Fig. 12(e) in [48] and is explained by the lower overlap of the mode with the vertical sidewalls. Both configurations are illustrated in Fig. 7(a) and (b). The consequence of this improved design is the lower confinement of the mode in the silicon waveguide resulting in an increased bending loss and thus limiting the maximum achievable FSR. Similarly, one can use a rib waveguide defined by a partial etch, which also has less sidewall surface, and weaker confinement [20].

Also, sidewall treatments can reduce the roughness, and in turn reduce propagation losses [42, 49]. Or by using thermal reflow techniques the waveguide core can be reshaped, resulting in a smooth curved surface of which the shape is dictated by surface tension [50].

Additional sidewall-induced loss mechanisms include dangling bonds which introduce surface state absorption. For high powers, two-photon absorption and free carrier absorption contribute to the non-linear absorption (see Sect. 3.7) [51, 52]. Also, light can be coupled to radiative modes in the substrate, this substrate leakage decreases

exponentially with bottom cladding thickness [53]. For a bottom oxide of 2 μm, these losses are negligible for the TE ground mode and in the order of 0.001 dB/cm for the TM ground mode [43]. The fundamental lower limit of propagation losses is associated to Rayleigh scattering, caused by deep sub-wavelength index perturbations in the bulk of the waveguides. When using high-quality crystalline SOI material, Rayleigh scattering inside the waveguide core material is expected to be extremely low.

The strong modal confinement (for TE-polarization) in SOI wires allows for very sharp bends (radius down to 3 μm) with still low radiation as compared to bends in conventional waveguides (radius down to 100 μm). However, both the substrate leakage and scattering loss might be influenced by waveguide bending, as the mode is pushed outwards (more with sharper bends). Excess bending losses of a 500 nm wide SOI waveguide amount to 0.01 dB/90° for a 4.5 μm bend, to 0.071 dB/90° for a 1 μm radius bend [19]. This excess bending loss of a circular 90° bend includes mode mismatch at the straight-bend interface, coupling between TE and TM modes, as well as higher order modes in the bend section and propagation loss in the bends. As bends are an essential component of a ring resonator, the excess bend loss should be kept under control. This can be accomplished by tuning the waveguide cross section [54] or by engineering the bend shape [20].

The patterning process itself can also introduce unwanted effects depending on the density of the structures. During lithography, (optical) proximity effects can introduce linewidth changes which depend on neighboring structures, and during etch, the etch rate can vary based on local density (so-called *loading* effects). This is especially relevant in the coupling section, where proximity effects can result in a rather abrupt change in line width when the waveguides come close together [19]. Also, the loading will impact the line width but also the uniformity of the ring resonators [42, 55].

While in general TE-light is the preferred polarization, as TE is the ground mode of the waveguide, there are advantages to using the TM mode: Because of its lower overlap with the sidewalls, it will experience less scattering, but more essentially, less backscattering. It has been successfully demonstrated to achieve high-Q microdisk resonators [28] (whispering-gallery modes) and microring resonators [31]. Using TM-polarized light in a waveguide cross section of 500 nm × 220 nm, as shown in Fig. 7(c), more than an order of magnitude less scattering loss is expected, based on [48]. This is a result of two effects: First, the electrical field of the TM mode is oriented mainly in the vertical direction, so no discontinuity is created on the vertical sidewalls. Secondly, the TM mode is less confined in the vertical direction ($n_{\text{eff}} = 1.89$), which results in a smaller modal overlap with the vertical sidewalls. Theoretical predictions by [48] have been verified by backscattering measurements in [29].

Because of the high index contrast, silicon wires are highly dispersive. This means that the effective index of the propagating mode is wavelength dependent, so monochromatic waves of different wavelengths will travel through the waveguide with different velocities. This causes propagat-

ing pulses (that comprise a sum of monochromatic waves) to broaden and to be delayed (more than due to ordinary waveguide dispersion). An SOI photonic wire has a normal first-order dispersion in the wavelength range of interest and for the dimensions we performed the characterization on: $\frac{dn_{\text{eff}}}{d\lambda} < 0$ [43, 56, 57]. At $n_g \approx 4.3$, the group index is almost twice as large as the effective index. This has a large impact on the spectral characteristics of a ring resonator.

Also, because of the high index contrast and small core size, photonic wires are exceptionally sensitive to dimensional variations. In [42,43] the effect of width and thickness changes on the effective index is analyzed. As discussed above, this is relevant to ring resonators as the effective index determines the optical roundtrip length.

3.2. Directional couplers

The most common way of coupling light from a waveguide to a ring resonator is through a directional coupler. In a directional coupler, two waveguides are brought close together: This can be done either in a horizontal (side-by-side) arrangement [58, 59] or in a vertical arrangement [60]. Alternatively, multi-mode interferometers can be used [61].

As we discussed, the coupling between the bus waveguide and the ring needs to be well controlled to design ring resonators with the desired spectral features. Therefore, a good understanding of the coupling section is crucial. Especially for multistage ring resonators (see Sect. 3.4), the design of reproducible directional couplers is one of the main bottlenecks to achieve accurate operation. As silicon photonic wires are very sensitive to variations, we expect similar effects in directional couplers.

A typical SEM cross section is shown in Fig. 9. Their theoretical behavior is well documented [62, 63], however few experimental studies are reported in literature. The coupling between two straight waveguides can be derived in a rather straightforward way, but in reality a directional coupler will also contain a section where the two waveguides are brought together. We can determine the full coupling of a directional coupler experimentally from ring resonators [64], but it is also possible to experimentally measure the coupling strength.
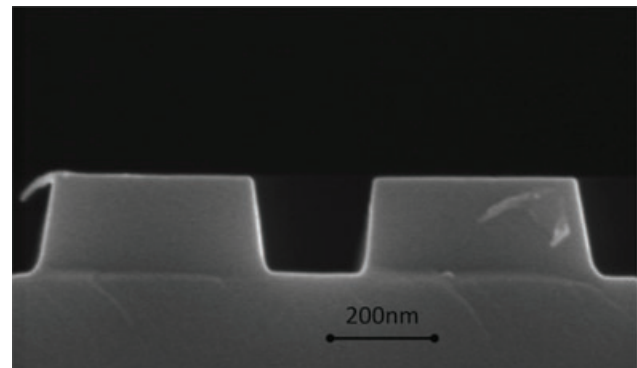

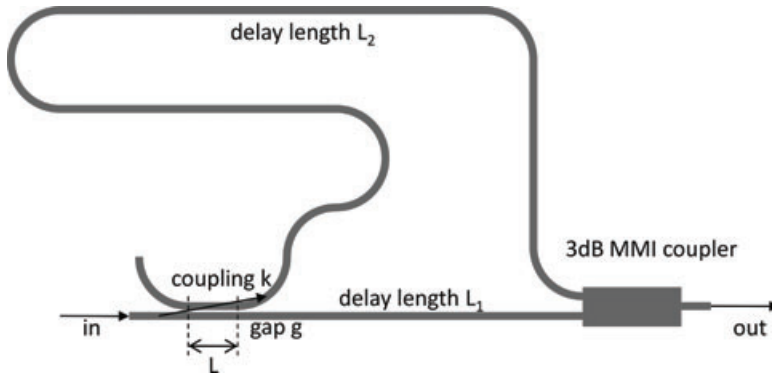**Figure 9** SEM cross section of typical SOI directional coupler.

Figure 10 A Mach-Zehnder Interferometer (MZI) was used as a test device for the study of directional waveguide couplers. From the adjacent minima and maxima of its spectrum we can extract the coupling coefficient of the splitter or combiner.

This can be done by introducing the coupler as the splitter or combiner of a Mach-Zehnder interferometer (MZI). The combiner is a symmetric 2×1 MMI which inherently will give a balanced combination (but for unintentional asymmetries introduced by fabrication). The concept is illustrated in Fig. 10. Because of the delay line, the MZI transmission will go through minima and maxima when sweeping the wavelength. When both the splitting and combining ratios are balanced, complete constructive and destructive interference will occur, and the minimum will have zero transmission. If the splitter is not perfectly balanced, we can extract the imbalance from the wavelength dependent ratio between adjacent minima and maxima of the output spectrum. When calculating the transmission of the entire device, we obtain [65]

$$E_{\text{out}} = \frac{1}{\sqrt{2}} jke^{-j\phi_1}E_{in} + \frac{1}{\sqrt{2}}\sqrt{1-k^2}e^{-j\phi_2}E_{in},$$

$$I_{\text{out}} = |E_{\text{out}}|^2 = \frac{1}{2}\left(1 + 2k\sqrt{1-k^2}\sin(\Delta\phi)\right)I_{in}.$$

With $\phi_1 = \beta L_1$, $\phi_2 = \beta L_2$ and $\Delta\phi = \phi_1 - \phi_2$. The directional couplers are assumed to be lossless in this calculation. As the coupling ratio of the directional couplers is wavelength dependent (especially for longer couplers), the extinction ratio (ER) between adjacent minima and maxima will vary as a function of wavelength, and can be extracted by fitting envelopes on the minima and maxima of the transmission of the MZI. From the ER we can calculate the wavelength dependent amplitude cross-coupling coefficient k:

$$ER = 10^{\frac{ER_{dB}}{10}} = \frac{\frac{1}{2}+k\sqrt{1-k^2}}{\frac{1}{2}-k\sqrt{1-k^2}} \qquad (27)$$

$$\Leftrightarrow k^2 = K_\pm = \frac{1}{2} \pm \frac{1}{2}\sqrt{1 - \left(\frac{ER-1}{ER+1}\right)^2}. \qquad (28)$$

By now sweeping the coupling length (L) of the directional couplers, we can extract the coupling strength per unit of length, as well as the residual coupling induced by the bend sections, and this as a function of wavelength: The L sweep can be used to fit the power coupling coefficient to a sine squared and obtain the coupling coefficient per unit distance $\kappa[1/\mu m]$ and the offset coupling coefficient due to the bend sections κ_0:

$$K(\lambda) = k(\lambda)^2 = \sin^2(\kappa(\lambda)L + \kappa_0(\lambda)).$$

This is only valid in the case where the coupling section is symmetric (i. e. both waveguides are identical), but the derivation could be expanded to asymmetric coupler sections. The fitting to a $\sin^2$ can also produce ambiguous results which can be eliminated with proper data fitting.

In [65] the coupling efficiencies are extracted in this manner for oxide-clad and air-clad directional couplers around 1550 nm wavelength, for 4 different gaps. The results are for 427 nm wide waveguides and gaps between 195 nm and 260 nm. This result is reproduced in Fig. 11. As expected, the coupling-per-length κ increases with longer wavelengths because of the lower mode confinement of the waveguide. For the same reason, the coupling for oxide-clad waveguides is higher than the coupling for air-clad waveguides. The residual coupling κ_0 is very sensitive to dimensional deviations, wavelength and fitting errors and hence shows a larger variation.

Good couplers are required to design rings with a good extinction ratio, as in that case critical coupling is required. In [66] a elaborate parameter study of ring coupling sections is performed to design good coupling sections for different ring and waveguide geometries.

3.3. Single silicon ring resonators

3.3.1. Characterizing a resonance

In Fig. 12 we show the transmission spectra around one of the resonance wavelengths at the pass, drop and add port of two microring resonators with gap of resp. 200 nm and 400 nm and a 5 μm radius. The spectrum is scanned using a tunable laser with 1 pm resolution, and fitted to a Lorentzian with a least-squares fitting method and scaled before determining the FWHM and the extinction parameters R_{min} and T_{max}. Both microrings consists of the waveguides with the cross section depicted in Fig. 7(a) and have symmetric coupling sections. We use the TE mode of the waveguide. The 5 μm radius fixes the FSR to ≈ 17–18 nm.

Using similar techniques as in [67] we can estimate the loss and coupling coefficient for the 200 nm gap ring. Assuming symmetric coupling and neglecting the backscattering we get $a = 0.97$, $k^2 = 0.10$. For this ring, $\lambda_{3dB} \approx 200\,pm$, which results in a Q-factor of $\approx 8 \cdot 10^3$. There is 5 dB difference in insertion loss (IL) between add and drop port. As
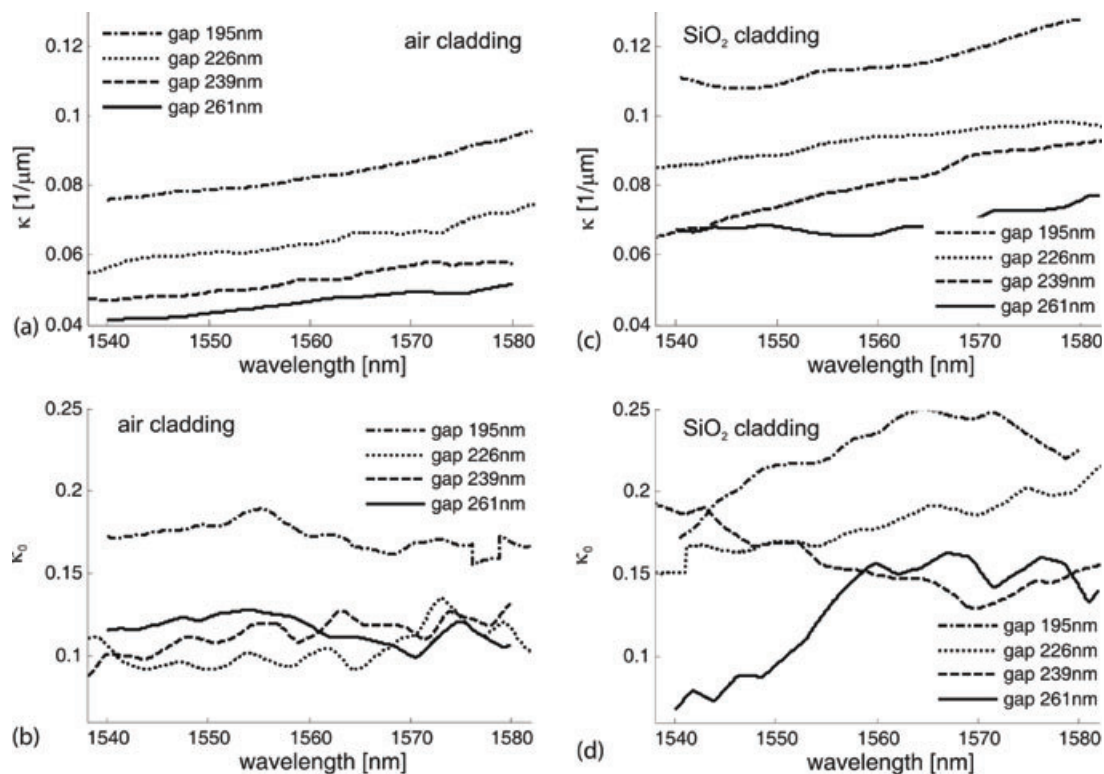
Figure 11 Experimental extraction of directional coupler efficiencies based on the structure in Fig. 10. Measured coupling coefficient per unit length $\kappa\,[1/\mu m]$, initial coupling coefficient κ_0 and beat length $L_{\frac{\pi}{2}}$ versus wavelength. Waveguide widths = 427 nm, top two graphs: air cladding, bottom graphs: SiO$_2$ cladding. Reproduced from [65].
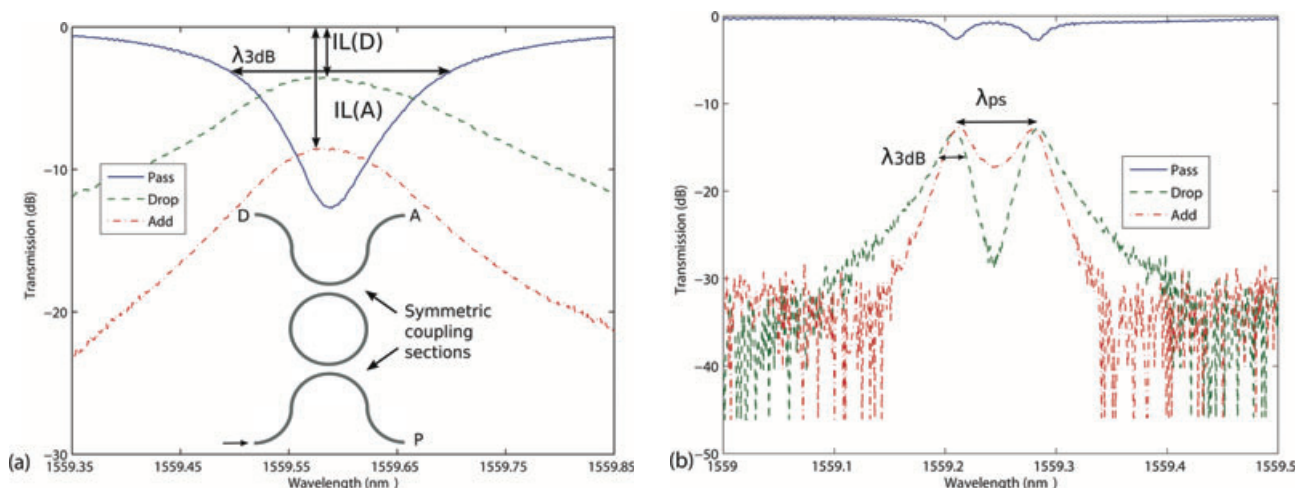

Figure 12 (online color at: www.lpr-journal.org) Spectra at the pass, drop and add port for a microring resonator with radius 5 μm and a gap of (a) 200 nm and (b) 400 nm using TE-polarized light and with cross section depicted in Fig. 7(a). In (b) the Q-factor becomes high enough to see resonance splitting. Moreover the output power level at the add port becomes comparable with the output power level at the drop port.

this difference in IL is still not that high we expect to see some peaksplitting, but the broader λ_{3dB} makes it difficult to resolve this. In this case R will be slightly smaller than k^2.

As the gap increases, coupling decreases, which causes an increase in Q-factor: we get a Q-factor of $\approx 8\cdot10^4$ for the 400 nm gap ring. For this ring we clearly see resonance splitting, which makes the determination of k^2 and a more

difficult. The resonance splitting of $\approx 70\,pm$ is broader than the 3dB-bandwidth $\lambda_{3dB}\approx 20\,pm$, so we can clearly resolve two peaks in the spectrum, which means $R > k^2$. Backreflection is clearly non negligible for this coupling geometry, as besides the resonance splitting also the insertion loss at the add port is of the same order of magnitude as the insertion loss at the drop port. Thus not only the spectrum is consid-

erably disturbed, but also the direction of the power flow in the microring is heavily modified. Similar remarks hold for the other resonance peaks in the spectra of both rings. These two examples clearly illustrate backscattering is a major issue when trying to design circuits based on high Q-rings.

3.3.2. FSR and group index

The group index can be determined experimentally by measuring the FSR of ring resonators with various round trip lengths: the test device is a rounded rectangular resonator (bend radius 4.5 µm), with a variation of the vertical straight section, while the coupling sections of 2 µm remain unaffected. Figure 13 shows the FSR as a function of the round trip length of a racetrack add-drop resonator. The waveguide dimensions are 450 nm × 220 nm. The group index n_g is determined by fitting formula (9) to the measured values of the FSR (measured $n_g = 4.30$). In Fig. 14 we see the change in Q factor with the length of the ring, as we expect from (22).
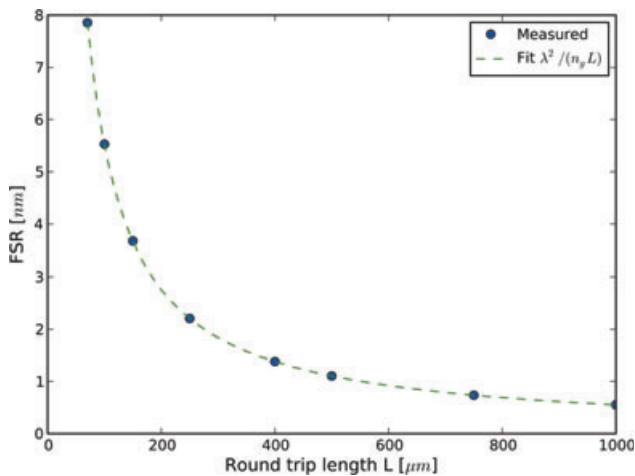

Figure 13 (online color at: www.lpr-journal.org) FSR plotted as function of roundtrip length. We see the FSR $\sim \frac{1}{L}$ behavior from formula (9) corresponding to an n_g of 4.30.
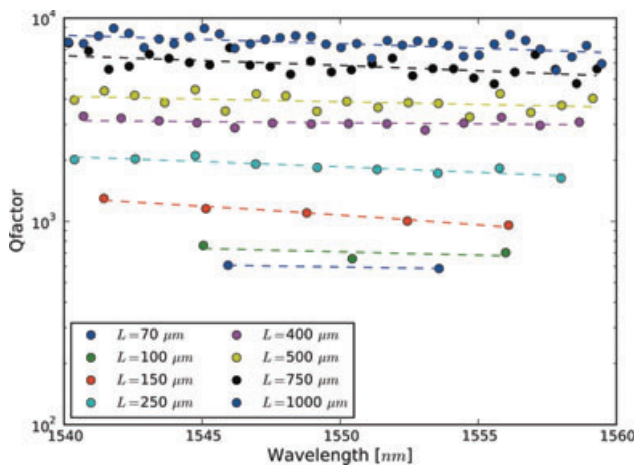

Figure 14 (online color at: www.lpr-journal.org) Q as function of wavelength for different ring lengths, with a coupler gap of 150 nm.

3.3.3. Losses and coupling

On the same set of devices we perform the analysis from Sect. 2.4, for different values of the gap width in the coupling section ($g = 150$ nm, 250 nm, 400 nm). We did not examine asymmetrical ring resonators because the error on measurements and fitting was too large to solve the system with three equations for a, r_1, and r_2. Therefore, we simplified the situation by using a symmetrical add-drop resonator. However, even then it is not straightforward to discriminate between the losses introduced by the coupling sections and those introduced by the ring itself. In an APF, a and r are even completely interchangeable, so it is not possible to distinguish them from the spectral characteristics. A first method to circumvent this issue was published by McKinnon et al. in [68]. They measure the transmission over a broad wavelength range and disentangle a and r based on how these parameters vary with wavelength. A second approach to solve this problem is, besides to determine the spectral intensity dependence of the microring, to measure the induced phaseshift of the resonator by inserting it in one arm of a nearly balanced MZI [16]. In an analoguous way, using the combined information from the measurement of an add-drop filter and a complementary APF (i. e. with the same coupling gap), it is even possible to make a distinction between the loss in the coupling section and the loss in the ring waveguides [67]. A drawback of the approach to calculate ring parameters using the combined information from measurement of different, although complementary, structures is that chip-uniformity problems can disturb the results [69]. A third manner to disentangle r and a is to measure parameter sweeps of rings which differ only in one parameter (in this case the length of the straight section, or the gap width in the coupling section). Figures 15 and 16 plot the Q and finesse as a function of roundtrip length, for rectangular rings where only the roundtrip length is varied by changing the straight section that is not coupled to a waveguide. The bend radius and directional couplers
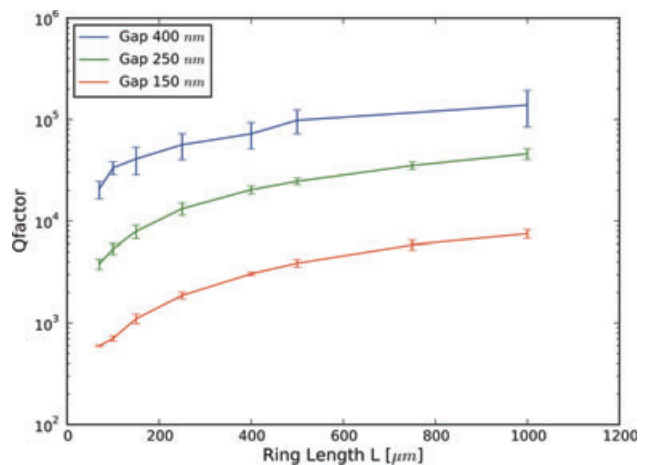

Figure 15 (online color at: www.lpr-journal.org) Q as function of roundtrip length, for rectangular add/drop ring resonators with different coupler gap widths. Error bars indicate variation over different peaks in the transmission spectrum.

Figure 16 (online color at: www.lpr-journal.org) Finesse as function of roundtrip length, for rectangular add/drop ring resonators with different coupler gap widths. Error bars indicate variation over different peaks in the transmission spectrum.
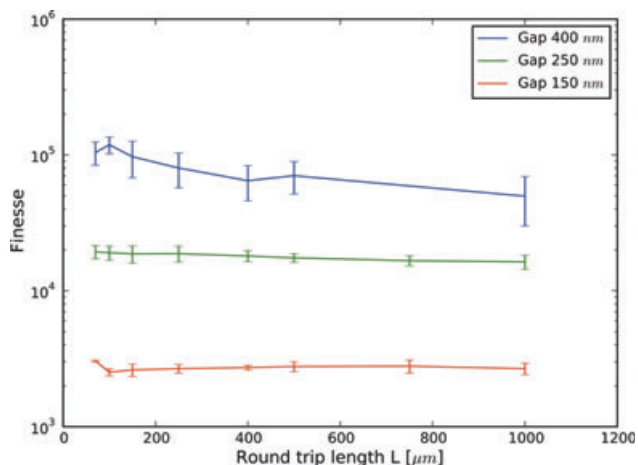
are designed to be identical. We performed this sweep also for different coupler gaps. We see a similar behavior as we got from the simple analytical model, where the maximum achievable Q is limited.

3.4. Multiple ring resonators

To achieve performant devices, devices with multiple coupled or cascaded ring resonators are often designed, such as for band filters, multi-bit delay lines, slow-wave devices and multiplexed or high-sensitivity sensor functionality. The parameters of the individual ring resonators and the coupling between ring resonators and input/output waveguides give the degrees of freedom to be used in the design to tailor the device characteristics to the required specification.

The Vernier effect is often exploited to create filters with an extended FSR. A number of groups have demonstrated silicon ring Vernier filters [70, 71]. Similarly, using two coupled rings with the second ring having 1–2 times the circumference of the first ring, Tobing et al. have shown a finesse enhancement compared to single-ring structures, with finesse up to 100 ($Q = 30000$) [72]. Inserting such a structure into a Mach-Zehnder interferometer (MZI) yields a sharp resonance with a reduced background envelope and increased contrast ratio (ratio between on-resonance and off-resonance transmission) [73]. However, careful balancing of the MZI structure is needed, which is difficult to achieve in practice. Darmawan et al. inserted also a single ring into one arm of a Mach-Zhender interferometer [74]. Such device can operate in two regimes, being a double-fano resonance mode or a single resonance mode, depending on the ring-waveguide coupling parameters. In such a double-fano resonance mode the parameters can be designed so that a flat box-like filter response is obtained.

The design of multi-ring resonator circuits in silicon requires knowledge of effects with a particular influence in silicon: ring matching [69], process biases [19] and coupling-induced frequency shifting (CIFS) [24].

The resonance matching of ring resonators in a multi-ring device plays a critical role. As will be discussed in Sect. 3.5, even in tailored process technology, the uniformity of ring resonators closely placed to one another is of the order of 0.5 nm. This of the same order as the typical channel spacing used in a WDM system or resolution required sensor devices. In cascaded ring devices, this will lead to faulty devices if the rings are not tuned or trimmed. In coupled ring systems, it will give rise to inhomogeneous broadening.

In multi-ring devices, the absolute and relative dimensions of coupling gaps between ring resonators and with the input/output waveguides plays an important role in achieving the required specifications such as on crosstalk or insertion loss. Nanometer-scale deviations on the coupling gaps will give a noticeable effect. When using projection lithography, waveguide couplers with different gaps will have slightly different dose-to-targets. Therefore, this should be taken into account during the design cycle [19, 75].

Coupling-induced frequency shifting [24, 64] is a third well-known effect, related to the phase response of ring-waveguide (or ring-ring) couplers, which is particularly severe in silicon rings. Several research groups are still studying these effects as new models are needed to understand and predict CIFS [76, 77].

When adding ring resonators to a single bus waveguide on a fixed interval, one can create a *side-coupled integrated spaced sequence of resonators* (SCISSOR) [78], where it is possible to tune the dispersion and slow down light. As we can see in Sect. 4.2, it is possible to use them as an optical buffer. Also, complex filters can be constructed in this manner [79].

3.5. Sensitivity and uniformity

One of the major issues in using a high index contrast technology such as SOI for photonic devices is its sensitivity to dimensional variations. Deviations in the width or the height of the devices will cause a proportional shift in the spectral response (see Eq. (24)). Even within a chip, ring resonators which are designed to be identical may not have an identical spectral response after fabrication. This is a consequence of non-uniformity in the fabrication process in lithography and etching, resulting in a variation in width and height of the photonic wire in the resonator. In a ring resonator addition, the coupling gap uniformity also plays an important role [24, 64]. It is important to note that for uniformity, the average width and height of the devices should be matched over the circumference of the ring, rather than the absolute local width and height. This means the average n_{eff} over the length of the cavity between two rings should be matched. The high contrast of silicon wires makes the waveguides so sensitive that variation in the ring dimension (width, height and coupling) due to mono-layers of atoms can be measured from the spectral response. Figure 17 shows a measured spectral response non-uniformity between two nominally ring resonators closely place with a chip to be smaller than that of a monolayer of silicon. The non-uniformity in the spectral response not only affects a single discrete device
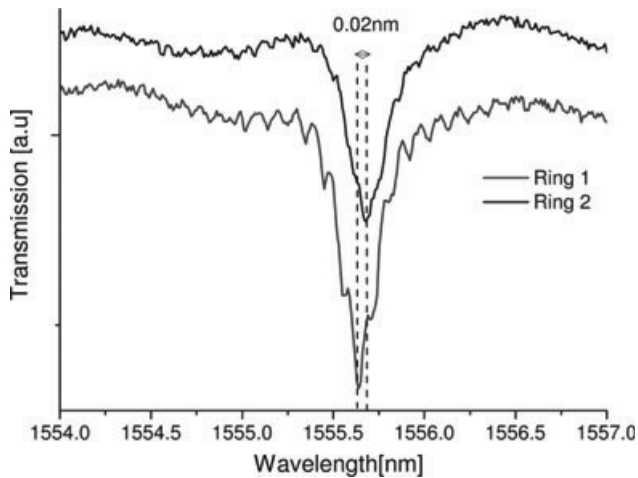
Figure 17 Spectral response of two nominally identical APF rings within a chip.

but also coupled and matched multiple rings in a circuit, such as a higher order ring filter [80].

The fabrication process is considered as the major cause of non-uniformity in the spectral response. It has already been demonstrated that within a chip a device uniformity within < 1% is achievable by making use of advanced patterning and process design [69]. In [69] and [55] we have shown that the device non-uniformity depends on various factors such as mask errors, process non-uniformity within a chip and over a 200 mm wafer.

Also, within a chip, that is in a short distance scale (few 10s of μm), the local density of devices has greater influence than the global variations [55]. Figure 18 shows the shift in the resonant wavelength shift as a function of distance between ring resonators which are optically decoupled. Despite the optical decoupling, we observe a blue shift in the resonant wavelength when the rings are closely spaced. This shift recovers to the spatially isolated response when the rings move further apart. The change in resonant wavelength
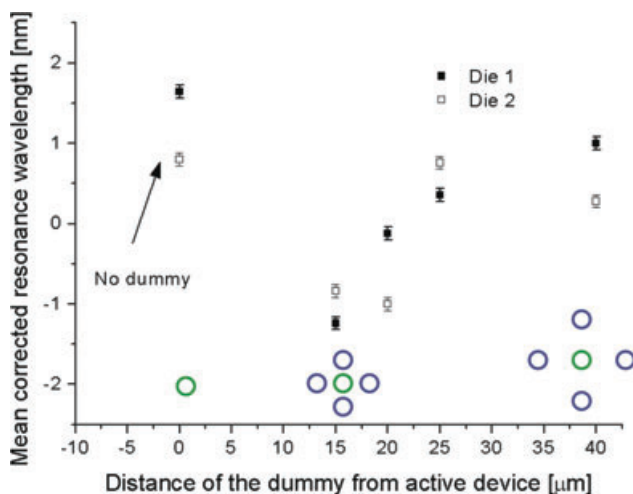

Figure 18 (online color at: www.lpr-journal.org) Effect of device density on the absolute wavelength response of a ring resonator.

is a consequence of local density variation which in turn affects the dry etch plasma process. This is often referred to as loading [81, 82]. Hence it is not only the fabrication process variation that influences non-uniformity in device but also the circuit/device density. Thus it is important that these factors are taken into account while designing matched ring resonators in a circuit. In CMOS circuits this issue is overcome by balancing the density of the devices over the chip by using dummy structures. This technique can be applied to photonic circuits as well.

3.6. Tuning and trimming

As mentioned above variation in device dimensions due to fabrication process variation is inevitable. A solution to overcome these variations is either trimming or active tuning of devices.

The resonance wavelength of a ring resonator can be actively tuned in several ways. Thermal tuning is the most widely used technique, because of the large thermo-optic response of silicon. Thermal tuning exploits this to the effective index and thereby the spectral response, according to Eq. (24). Figures 19a and b show the drop spectrum and resonance wavelength shift of a 2nd order ring filter as a function of temperature respectively. In this case, the thermal energy was supplied to whole chip. However, in practice each device requires an individual heat source to address them separately. This is achieved by using micro-heaters, which can be placed either at the top or at the side of the device as a heat source with sufficient isolation to avoid optical loss. The most common heater configuration is placing the heater on top of the device [83–88]. However, other configurations such as a lateral placement can also be realized using CMOS processes [89].

Since the size of the micro-heater depends on the resonator size the efficiency is compared in terms of power required to detune the ring over its entire FSR [Watt/FSR]. This efficiency (lower values are better) depends on the heater material, heater layout and the thermal conductance of the material between the heater and the device. Micro-heaters are usually made using high-resistivity metals such as Titanium, Platinum, Nickel, Chromium and alloys of these metals. For instance, in the case of Titanium, the heater is often covered with gold or silicon dioxide to avoid oxidation of the metal at a higher temperature, which might result in poor reliability. Silicon dioxide, which is one of the most widely cladding/isolation material on which heaters are fabricated, has a very low thermal conductivity (1.38 W/mK) [90]. This has the advantage of limiting thermal crosstalk between neighboring heaters, but the disadvantage that the actual heat reaching the waveguide is relatively small. Despite this disadvantage, efficient heaters were demonstrated by clever design and additional post-processing. For an efficient heater, the transfer between the heater and the device through the isolating materials should have high thermal conductivity and at the same time the optical properties similar to silicon dioxide. It has been shown
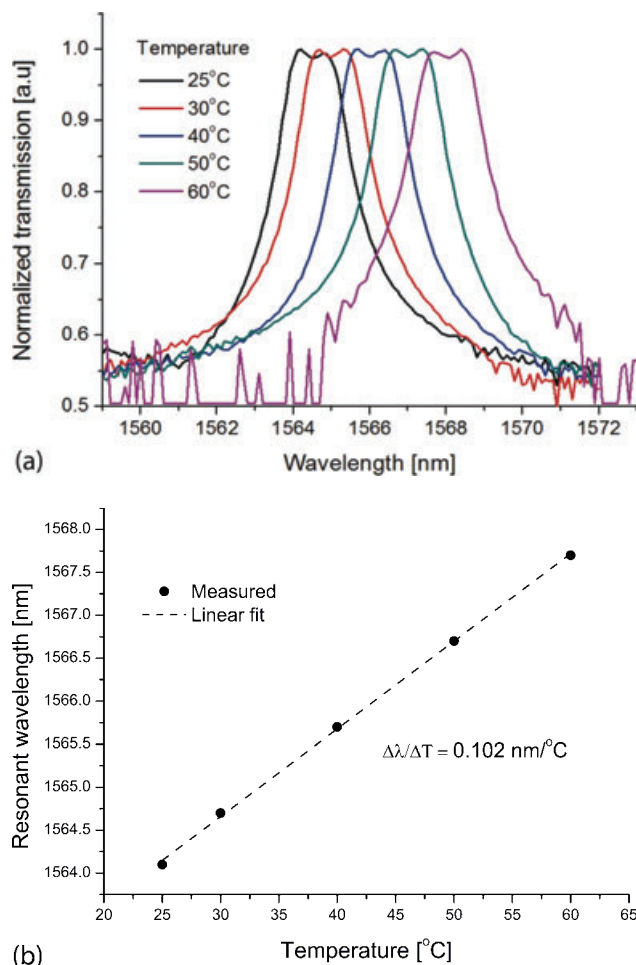
Figure 19 (online color at: www.lpr-journal.org) Thermo-optic tuning. (a) Shift in drop response of a 2nd order ring ring filter and (b) wavelength shift as a function of temperature.

that such properties are possible with hybrid nanocomposites containing BCB and diamond nanoparticles mixtures with high thermal conductivity [91]. Another way of improving the efficiency is through better heater layouts. It has been shown that by using spiral resistive heater with efficient heat spreading design tuning powers as low as 20 mW/FSR have been demonstrated [92]. This efficiency can be further improved by reducing the heat loss and confining the heat flow to the device, which resulted in an efficiency of 2.4 mW/FSR but with a slow tuning speed of 170 µs [86] . A similar approach was followed in [93], where the silicon substrate was removed to improve conduction loss.

While thermal tuning is used to actively tune the resonance wavelength of the ring resonators, post-fabrication resonance trimming can be done to permanently change the spectral response of the resonator. Trimming of devices requires a permanent change in the effective refractive index through change in material property, mainly refractive index of the core or the cladding material. Since crystalline silicon is a physically passive material, trimming the refractive index without adverse optical effect is difficult. Hence trimming is mostly applied to the cladding material. It has

been shown that by trimming the cladding refractive index either by using photo-oxidation of polymer cladding [94] or by inducing stress to BOx layer [95].

The advantage of trimming is that it can be done at the end of the fabrication process, and subsequently the rings can be modified to obtain an athermal behavior. This can be accomplished by combining the silicon with a cladding that has an opposite thermo-optic constant (i. e. most polymers) and engineering the waveguide cross section to balance the confinement in the core and the cladding [96]. However, this typically involves quite narrow waveguide, which have poor confinement and thus do not allow sharp bends.

3.7. Nonlinear effects in rings

Silicon photonic wires are an ideal platform for nonlinear photonics [97–100]. This because the tight confinement gives rise to high power densities for modest overall power, and also because silicon exhibits some (but not all) strong nonlinear effects. Some of the third-order ($\chi^{(3)}$) nonlinear effects that have been observed in SOI waveguides include stimulated Raman scattering (SRS) [101–103](useful for amplification [104–107] and even lasing [108–110]), the Kerr effect which gives rise to self-phase modulation [111] or cross-phase modulation [112]. Two-photon absorption (TPA) can also be used for cross-phase modulation and cross-amplitude modulation [51, 52]. On top of those direct nonlinear effects, there come a number of secondary effects into play. TPA gives rise to additional free carriers, which in turn will absorb light (*free carrier absorption* of FCA) and introduce additional *free carrier dispersion* (FCD) [113]: effects which have been demonstrated to be useful for switching [51, 114]. Thermalization of the free carriers will generate heat in the waveguide, which gives rise to thermo-optic effects [115]. Silicon exhibits no native second-order nonlinearities, as it has a centro-symmetric lattice structure. However, it has been shown that breaking this symmetry by inducing strain gives rise to non-zero electro-optic effects [116].

Naturally, in a (ring) resonator these effects become more pronounced, as close to resonance we will see a strong increase in power density. In magnitude, the thermal effects are actually dominant, but they are slow. Bistable behavior has been demonstrated in silicon microring resonators [117, 118]: the increased optical power will result in a skewing of the resonance peak. This is illustrated qualitatively in Fig. 20 for the drop port transmission of an add-drop filter. At a certain power level, the resonance peak will fold back, resulting in three possible transmission levels, of which only two are stable solutions. This means that the ring transmission spectrum at such power levels will differ whether it is measured from long to short wavelengths or from short to long wavelengths (when using a swept laser source). Similarly, there will be hysteresis in the power transmission at a wavelength in the bistable region. The power requirement for thermal bistabilities depend on the Q of the ring.
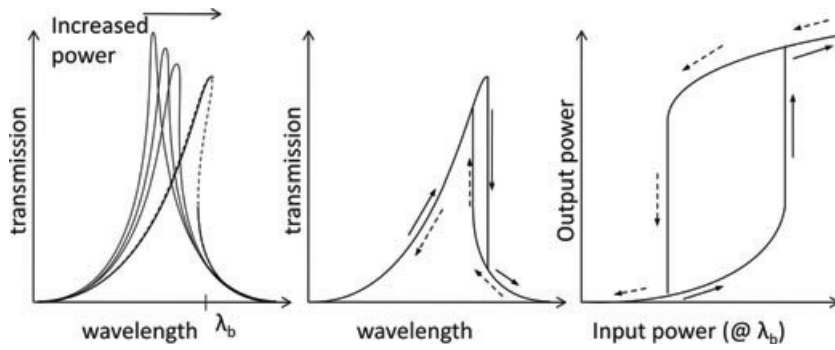
Figure 20 Nonlinear bistability in ring resonators. (a) skewing of the resonance at higher power levels, (b) hysteresis in a wavelength sweep, (c) hysteresis in optical resonance at a fixed wavelength.

The thermal nonlinearities translate the optical power into a phase shift. A similar effect occurs with the free carriers generated through TPA. The resulting free carriers can be used in a ring resonator to induce a non-linear change in the real part of the refractive index [115, 119]. These carrier effects are much faster than thermal effects. When combining both effects with a different time scale, this can result in self-pulsing behavior [120].

By definition, nonlinear effects will generate additional frequency components in a signal. As silicon has no intrinsic second-order nonlinearities, there will be no generation of second harmonics. However, the third-order nonlinearity (Kerr effect) is quite strong, and the resulting green emission of third-harmonic generation has already been demonstrated [121]. This also means that wavelengths in a waveguide are no longer independent, and that nonlinearities will generate new wavelengths through four-wave mixing (FWM) [122]. In FWM, two pump photons interact and result in two new photons (a signal photon and an idler) at different frequencies [123]. This can be used for wavelength conversion [124–127] and all-optical signal processing [128, 129]. Obviously, the total energy of the new photons should be the same as the energy of the original photons. Also, the signal and idler photons are correlated: This means the processes can also be used to generate entangled photons [130, 131].

In degenerate FWM, the two pump photons have identical wavelength, and the signal and idler are spaced evenly in the spectrum on both sides of the pump. This means that a single high-power pump will experience some spectral broadening as it travels through a non-linear waveguide [132]. However, for this effect to add up constructively over the length of the waveguide, the group velocity n_g should be constant over the entire relevant wavelength band. To obtain this zero group velocity dispersion (GVD), the waveguide geometry should be engineered such that the geometrical dispersion counteracts the material dispersion. When using FWM in a ring resonator, the effect will be strongly enhanced by the cavity when the interacting wavelengths are on resonance in the ring. This means that the FSR of the ring should be really constant, putting the same restriction on the group index. In such a ring resonator, the FWM will now generate a comb of evenly spaced wavelengths [133]. At this time, no sizeable frequency combs have been demonstrated in silicon waveguide ring resonators.

Nonlinear effects can also generate interesting phenomena in coupled rings. For instance, in a SCISSOR consisting of all-pass ring filters on the same bus waveguide, it is possible to excite solitons propagating from one ring to the next [78].

4. Applications of ring resonators

Their simple concept and geometry makes ring resonators usable for a variety of applications. As a resonator, they can serve as spectral filters, which can be useful for communication purposes. This is especially true if the rings can be tuned. Also, because ring resonators store the optical energy in a resonance, they could be employed in optical delay lines. We discuss both these applications in somewhat more detail.

We already discussed the sensitivity of silicon microrings, and this makes the devices ideal for a variety of sensing microring applications. In essence, the shift in resonance wavelength can be used to sense anything that affects the optical properties of the silicon core or the cladding. This can be temperature [96] (silicon has a quite strong thermo-optic constant), or index changes due to changing composition of the top cladding [135]. They can even respond to direct physical deformation [136] and be used as a strain sensor. However, the use as sensor becomes more relevant when introducing selective mechanisms, which amplify the ring's response to a specific effect. This can be done by chemically modifying the ring surface, to respond to e.g. specific gasses [137, 138]. However, the largest potential is in the combination with biochemistry to make sensors for specific biomolecules.

The final application which we will cover in more detail is the use of active ring resonators, where an active section is incorporated in the ring. This could be a fast phase shifter to shift the resonance, to make a modulator [139–141], or it could be a gain or absorption spectrum, to make a ring laser [142] or resonant detector [143], respectively.

4.1. Spectral filters and switches

Ring-based spectral filters are useful for telecommunication and data communication purposes to multiplex or demultiplex WDM signals. Several techniques exist for such
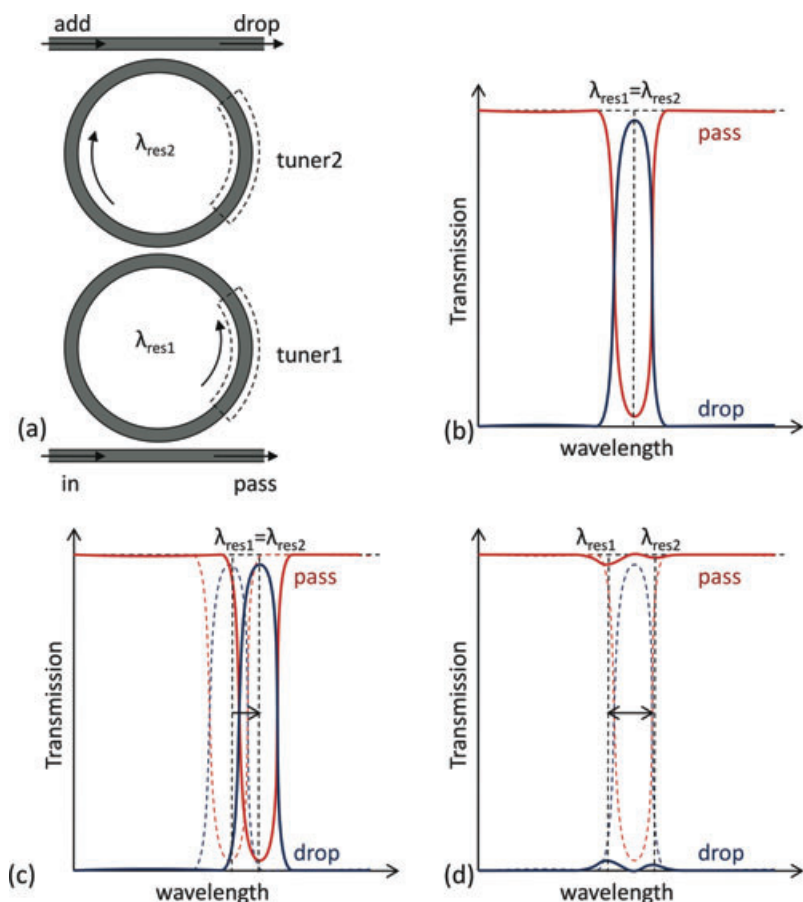
Figure 21 (online color at: www.lpr-journal.org) Principle of a wavelength-selective hitless filter switch [134]. (a) Two-ring switch concept (b) Response in drop operation, (c) wavelength tuning by driving the tuner in the same direction, (d) switching to pass operation by driving the tuners in opposite direction.

multiplexers, ranging from interleaved MZI filters [6] to all-out (de)multiplexers based on arrayed waveguide gratings [6, 7] or echelle gratings [144, 145]. Ring resonators could also be used for banks of compact wavelength channel filters. However, while a good ring resonator could well meet the requirements for a WDM system in some circumstances, it will lack in tolerance to variations in fabrication and environmental changes (e. g. temperature), and this will require good process control to make the ring hit the exact wavelength without the need for large tuning currents [146]. Also, the shape of the resonance is far from ideal for a wavelength drop filter, and for high-speed signals (which have a bandwidth which is no longer negligible compared to the ring resonance width), the uneven pass band can introduce signal distortion [147].

Therefore, a higher-order filter is better suited for this purpose, as it can provide a more uniform pass band over a wider wavelength range, and at the same time have a larger extinction ratio outside the pass band [148]. Using a double ring resonator as a wavelength drop filter has an additional advantage: when both rings can be tuned individually, it becomes possible not only to move the resonance wavelength around (by tuning both rings in the same direction) but also switch the resonance on or off (by detuning the rings with respect to one another). This is illustrated in Fig. 21. This turns the rings into a wavelength-selective switch, which can drop a wavelength off a bus waveguide without disturbing the adjacent wavelength channels [134, 149].

4.2. Optical delay lines

Compact ring resonators are an attractive choice to realize optical delay lines or buffers in photonic integrated circuits [80, 150, 151]. Near resonance, the ring resonators will have a strong dispersion, and therefore a large group delay, storing the optical signal before releasing it. This large group delay, combined with a relatively large bandwidth and low IL provides an ideal combination for optical buffers. While the group delays generated by a single ring resonators are too small for practical applications, high order ring resonators can be used to increase group delay. Figure 22 shows the two most widely used delay line configurations: a SCIS-SOR consisting of all-pass filter, and a coupled resonator optical waveguide (CROW) [80, 152]. Temporal delay is not the only metric for an optical buffer. The achievable delay over a given bandwidth is also important. The delay-bandwidth product T is therefore the most relevant metric for optical delay lines: in a communication system it is a measure for the number of bits that can be stored by a buffer. For a single ring APF buffer it is given as [153]

$$T_{\mathrm{APF}} = \tau \Delta \lambda = \frac{(1 + \tau_0)}{\pi \sqrt{k}} \equiv 2/\pi \qquad (29)$$

where $\Delta \lambda$ is the normalized bandwidth, τ_0 is the maximum delay of a single ring, and k is the coupling between the ring and the bus waveguide. For an APF buffer equation T can be multiplied by the number of cascaded rings.
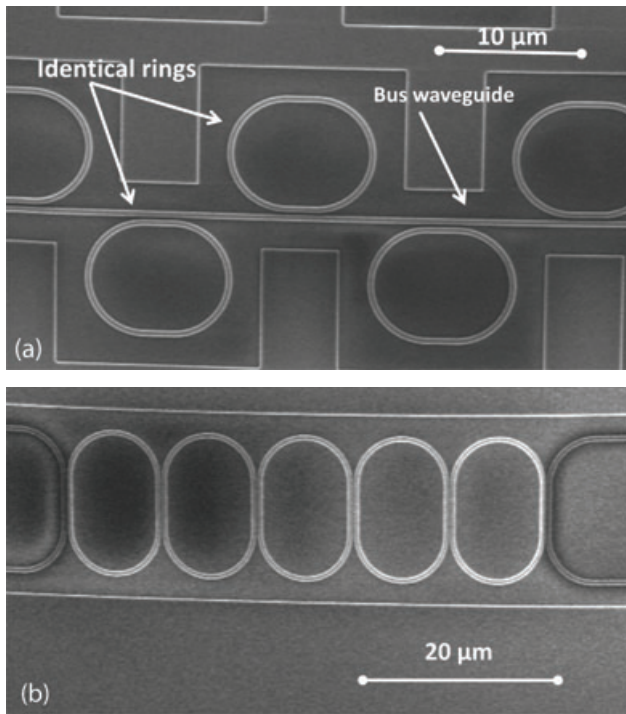
Figure 22 Scanning electron micrograph of (a) multiple APFs and (b) Coupled resonator optical waveguide.

For a CROW buffer, $T_{CROW} = N/2\pi$, where N is the number of cascaded rings. Figure 23a and b shows the measured temporal delay of a 50 ps pulse through APF and CROW buffer with a different number of cavities respectively. Using these configurations delays as large as 510 ps and 220 ps have been demonstrated in APF and CROW configurations, respectively [80]. These two configurations operate in two different modes. The APF is operated in bandstop(notch) mode, while the CROW is operated in bandpass(transmission) mode. Even though the APF configuration yields substantially higher delays, the IL at resonance is very high, making them impractical for implementing an optical buffer. CROWs, on the other hand, can be designed to have low IL with a moderate delay. In addition to the delay, the loss A induced by the resonator has to be taken in to account while comparing different buffer configuration. The figure-of-merit for a buffer can then be presented as,

$$FOM = \frac{\tau \Delta \lambda}{A} . \tag{30}$$

In an ideal case, the effective delay from a high order APF should be multiples of a single ring delay, however, non-uniformity in the rings result in resonance wavelength variation, which eventually reduces the effective total delay. As mentioned earlier the variation can be actively tuned to align the individual ring to a designated resonance wavelength. It has been shown in other material technologies that the buffer can be thermally tuned over a wide range of delays [151, 154–156]. These tunable delays allow the buffer module to be adaptable to different data rate signals, or delay lines that can be switched on or off at will. Note
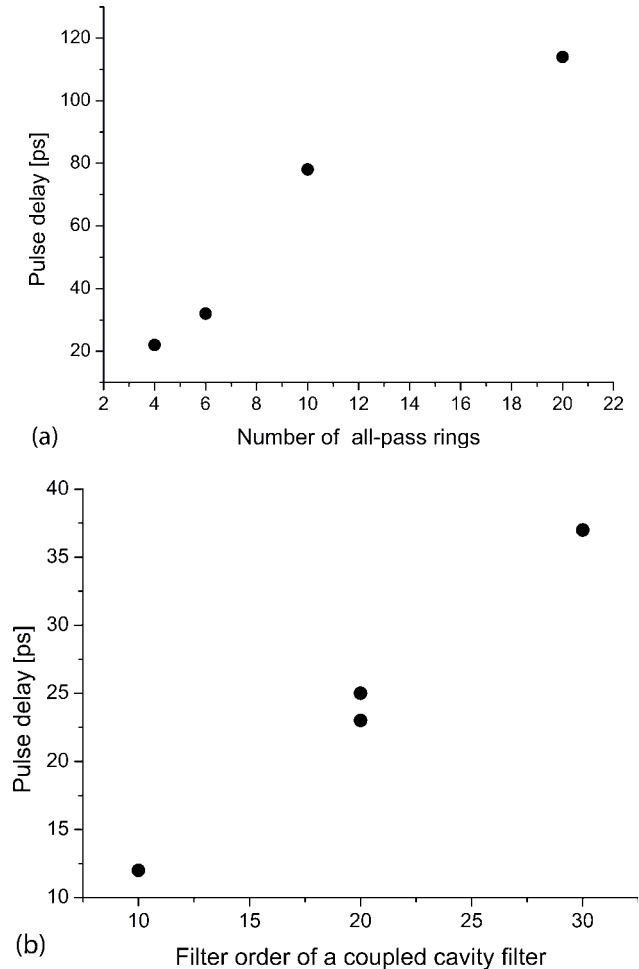

Figure 23 Measured delay of a 50 ps pulse through (a) an APF buffer and (b) a CROW buffer.

that this is again a fundamental difference between an APF delay line and a CROW. By detuning the rings in an APF, the delay line can be switched off, making it transparent with only the residual physical delay of the bus waveguide. In a CROW, this can also be accomplished, but imprecise detuning can have a detrimental effect on the overall transmission of the CROW.

It has to be noted that even though ring resonators are an ideal choice for implementing compact optical buffers, the usable bandwidth is limited. In case of broadband buffers other options such as, spiral photonic wires can be used [157]. However, the disadvantage is that they are not compact, which might cause implementation difficult on the circuit level, and the delay is not widely tunable.

For more details on the properties of coupled resonator optical waveguides, the reader can refer to a focused review paper by Morichetti et al. that is included in this issue [158].

4.3. Label-free biosensors

In medical diagnostics, drug development, environmental monitoring and food quality control there is an increas-
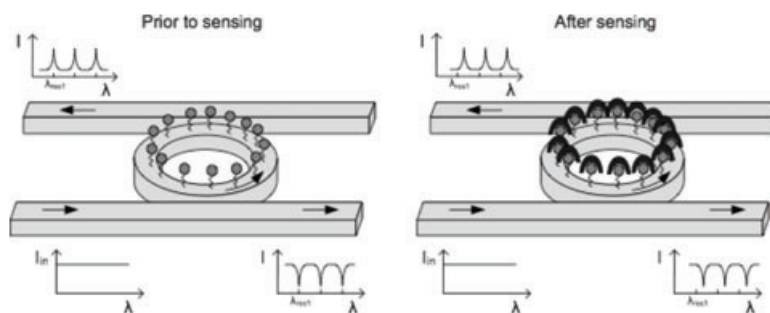
Figure 24 A label-free ring resonator biosensor has a chemically modified surface, so that receptor molecules that are selective to the analyte are immobilized on its surface. First an aqueous buffer solution is flown over the sensor to determine the reference resonance wavelengths, that are proportional to the effective roundtrip length of the resonator. Then the test solution is flown over the sensor, allowing analyte molecules to specifically bind to the immobilized receptors in the evanescent field of the resonator waveguide, causing an increase of the effective roundtrip length of the resonator and a corresponding increase of each resonance wavelength proportional to the number of binding events.

ing demand for biosensors that can specifically detect biological analytes in a fluid, such as drug compounds, DNA oligomers and antibodies. The necessary technological development is challenging because the analytes are often only a few nanometers large, can have concentrations down to the fg/ml-range and are typically present in a fluid that contains many other molecules at concentrations that are several orders of magnitude larger.

Nowadays, biological research typically relies on the indirect detection of an analyte by attaching an easy to measure label to it, such as a fluorescent dye. However, it is difficult to perform quantitative measurements with this method, it does not allow to obtain kinetic information of the biomolecular interaction and often requires intensive and expensive development of labels specifically for each target analyte. Therefore, label-free affinity biosensors have lately been receiving a lot of attention. They consist of a transducer with receptor molecules immobilized on its surface. In contrast to labeled detection methods, the transducer will respond directly to a selective affinity interaction between analyte molecules and the immobilized receptor molecules, allowing continuous and quantitative measurements [159, 160].

Silicon-on-insulator ring resonators are excellent transducers for label-free biosensing. First, they are highly manufacturable resonators of which the transmission spectrum heavily depends on the resonator's direct environment and that can be made with large quality factor, large extinction and low insertion loss. Second, they can be made very compact, allowing many of them to be incorporated on a single chip to perform simultaneous measurements of multiple analyte concentrations. Third, they can be made cheap when fabricated in high volumes with CMOS-compatible processes, so that the sensor chips can be disposable, meaning that the chip is only used once, avoiding complex cleaning of the sensor surface after use.

Figure 24 illustrates the concept of label-free biosensing with ring resonators. Prior to the measurement, receptor molecules that are selective to the analyte are immobilized on the resonator by chemically modifying its surface [161]. The resonator is designed to have a large extinction and can be an add-drop or an all-pass filter, of which the latter is usually preferred for being able to obtain larger quality factors. First an aqueous buffer solution is flown over the sensor to determine the reference resonance wavelengths, that are proportional to the effective roundtrip length of the resonator. Then the test solution is flown over the sensor, allowing analyte molecules to specifically bind to the immobilized receptors. The bound analyte molecules typically have a refractive index of 1.45 [162] and replace water with a lower refractive index of 1.31 in the evanescent field of the resonator waveguide. The resulting change of the effective roundtrip length causes an increase of each resonance wavelength proportional to the number of binding events, as defined by Eq. (25). By scanning the transmission spectrum of the resonator repeatedly with a tunable laser and measuring the resonance wavelength shift as a function of time, the concentration of the analyte and kinetic information about the binding of the analyte to the receptor can be determined. Typically, a Lorentzian function is fitted to each measured resonance dip or peak in order to determine the resonance wavelength in a noise tolerant way [65].

We can simplify the interaction of biomolecules to the surface of the waveguide as the deposition of a conformal adlayer with a certain thickness t_L and a certain refractive index n_L, as illustrated in Fig. 25. This allows us to construct a model to calculate the sensitivity for such interactions [65]. However, such models are approximations and a calibration with known concentrations of biomolecules on the surface will always be required.
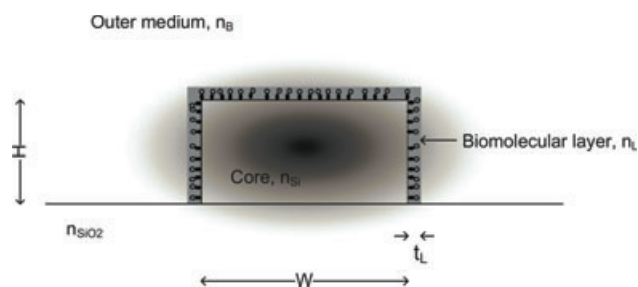

Figure 25 (online color at: www.lpr-journal.org) Optical model of a layer in which biomolecular interaction takes place.
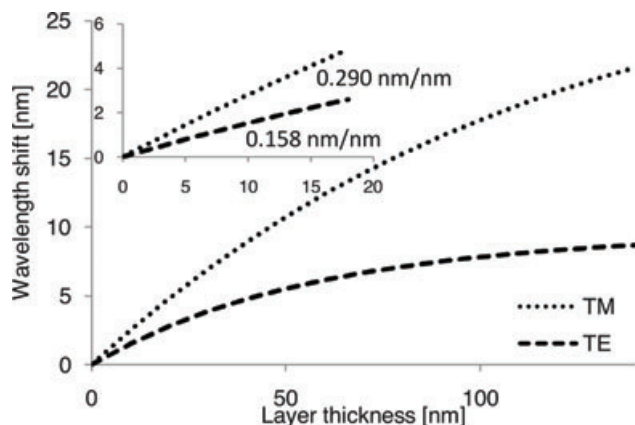
Figure 26 Wavelength shift $\Delta\lambda$ in function of layer thickness for a waveguide with dimension 480 × 220 nm. Reproduced from [65].

Figure 26 simulates the wavelength shift that occurs upon molecular interaction (and thus layer thickness t_L), using a mode solver and formula (25). In this case, $w = 480$ nm and $h = 220$ nm. For layer thicknesses up to 40 nm the sensor response is linear. This thickness is far beyond the thickness of molecular layers and thus forms no limitation. The validity of this model was verified experimentally [65]. From the graph in Fig. 26 the sensitivity for thin layers is determined to be 0.158 nm/nm for the TE mode, and 0.290 nm/nm for the TM mode. From Fig. 7 we know that the TM mode has a lower confinement, and this can explain the larger calculated sensitivity, but the lower confinement might also induce larger losses through bend radiation and absorption in the water cladding. For wavelengths around 1550 nm, the bulk absorption in water is as high as 10.9/cm [163]). This will have a dramatic impact on the attainable Q of the ring resonator, as can be extracted from Fig. 5. In Fig. 27 the calculated sensitivity is plotted for single mode waveguides with varying core width and fixed core height of 220 nm. Reducing the waveguide core dimensions will expand the waveguide mode, increasing the interaction with the sur-
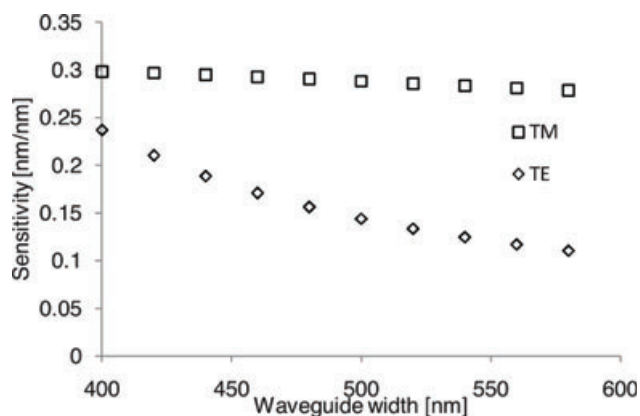

Figure 27 Surface sensitivity in [nm shift/nm layer thickness] for a layer ($n_l = 1.45$) in an aqueous solution on a 220 nm thick waveguide as a function of the core width of the waveguide. Reproduced from [65].

rounding cladding material and increasing the sensitivity. But pushing the mode outward will again increase water absorption losses.

For a sensor used in wavelength interrogation, the sensor resolution is the accuracy with which a wavelength shift can be determined, in other words, the minimum detectable wavelength shift $\Delta\lambda_{min}$. Together with the sensor sensitivity it determines the overall detection limit. $\Delta\lambda_{min}$ depends on the shape of the resonance spectrum, the noise, the fitting procedure and the measurement resolution [65].

An important characteristic of any sensor is its static detection limit, defined as the smallest quantity of the analyte that can still be detected. It is not only determined by the sensor sensitivity, a measure for how much the resonance wavelength shifts when molecules bind to its surface, but also by the amount of noise on the resonance wavelength signal [164]. The latter can be caused by index variations in the evanescent field of the sensor, small temperature variations and intensity or wavelength noise on the transmission spectrum, the impact of which is influenced by the extinction ratio and width of the resonance [165]. Shifts of narrow, sharp and deep resonances are more easily resolved when the transmission spectrum is susceptible to intensity and wavelength noise.

Published values of the detection limit are often determined with different methods, complicating a comparison. In the case of a biosensor, it can be expressed as the smallest detectable surface concentration of the analyte on the sensor surface (typically in pg/mm^2), with state-of-the-art values between 0.3 pg/mm^2 and 3 pg/mm^2 [166–168], which is already comparable with that of more mature label-free surface plasmon resonance sensors [169]. Due to the small size of silicon-on-insulator ring resonators, the corresponding absolute mass detection limit is very low. Reported values vary between 40 ag and 125 ag [166–168]. The detection limit can also be expressed as the smallest detectable volume concentration of the analyte in the test solution (e. g. in nanomolar or pg/ml), but this complicates a comparison even more, as it is also dependent on the mass transport of the analyte molecules to the sensor surface, the surface density of immobilized receptors and the affinity between analyte and receptor. A first aspect that has a positive impact on the detection limit, is a compensation of the temperature-induced drift with additional control ring sensors that are shielded from interaction with biomolecules by a cladding layer, but that are in thermal contact with the liquid [170, 171]. A second aspect which can considerably improve the detection limit beyond the static detection limit, is measuring the initial slope of the transient binding curve [171], in contrast to measuring the absolute wavelength shift at saturation. This method moreover improves the dynamic range and time to result.

Single-parameter measurements only provide limited detail and quantification of multiple biomolecular signatures can more fully illuminate complex biological functions [160, 169] An array of silicon-on-insulator ring resonator biosensors has already been applied to simultaneously detect multiple proteins [166, 167, 172] and oligonucleotides [171, 173].

To conclude, silicon-on-insulator ring resonators have in recent years been proven to be excellent transducers for label-free biosensing, comparing favorably with other label-free sensing techniques. The absence of a real need to integrate sources, modulators or detectors make this a very promising application for silicon photonics in the near future.

4.4. Active ring resonators

4.4.1. Modulators

Apart from using rings as passive devices, i. e. where they filter optical signals or act as a sensor, they can also be used as an electrically actuated device. In the past few years, a lot of work has been invested by several groups in electro-optic modulators based on ring resonators. In a ring modulator (or a modulator based on any resonator), the resonator is tuned such that the operating wavelength is on the slope of the resonance peak. By then modulating the optical length of the ring, the resonance peak is shifted and the transmission/reflection of the cavity is changed. This is illustrated in Fig. 28.

When using ring resonators, the most commonly explored configuration is a single all-pass filter close to critical coupling [140, 141]. In this configuration, there is a strong dip in the transmission spectrum of the bus waveguide, which means that a large modulation depth ER_{mod} can be achieved with a relatively small shift of the ring's resonance frequency. Obviously, the modulation is more efficient as the slope of the resonance is steeper, i. e. when the ring has a higher Q and finesse. Also, it is best to operate the modulator in the linear regime, i. e. where the slope of the resonance is close to a straight line. However, this implicates a penalty in modulation depth, and also introduces a certain IL. At higher Q, light is trapped in the ring for a longer time, and this will eventually limit the modulation speed of the ring. For fast modulators, rings with a Q of 5000–25000 are typically used.

The modulation of the effective index in the ring can be done with different mechanisms. We already mentioned that temperature can be used to this effect, but due to the relatively large time constants ($\sim \mu s$) this is not a suitable technique for fast signals. The most commonly used technique relies on manipulating the carrier density in the ring [174]. The refractive index and the absorption of silicon is influenced by the actual concentration of electrons and holes [113]. The most efficient mechanism in terms of magnitude is carrier injection in a p-i-n diode: The intrinsic zone is located in the waveguide core. By forward biasing the diode, majority carriers are forced into the core, strongly affecting the refractive index [2, 140, 175]. However, this mechanism is limited in operation speed by the recombination time of the carriers in the core ($\sim ns$). Better, one can start with a p-n diode in the core, which can be reverse-biased to increase or decrease the depletion zone in the junction. Because the effect moves around much less carriers, the effect is weaker, but it is also potentially much faster, as it is not limited by recombination times, but rather by the capacitance of the junction and the carrier saturation velocity [176–179]. Manipulating the carrier density in the ring will not only result in a modulation of the effective index, but also of the absorption. This, in turn, will have an effect on the Q of the ring [180]. When injecting more carriers, the Q will decrease, and thus also the slope of the resonance. In addition, changing the Q will also move the ring away from critical coupling, potentially reducing the achievable modulation depth.

An advantage of ring resonators for modulation is that they are quite compact and can be actuated directly as a lumped element, even at high speeds (10–25 GHz). Also, the relatively small area limits the necessary power to modulate. Therefore, ring modulators currently hold the best track record in terms of modulation energy per bit [139, 174]. However, it is essential that the edge of the transmission dip is spectrally aligned with the operating wavelength of the source. This will require good process control, but ultimately a tuning mechanism to compensate for external influences, such as thermal variations. The modulator could be tuned by applying a bias to the modulation voltage, but as the modulation effects are typically quite small, in most cases the tuning range will be too small. Adding thermal tuning will help, but it can only be used in one direction (heating not cooling). This means that, too compensate for thermal fluctuations in the chip, the operating temperature must be set near the upper boundary of the operation specs. This means continuous heating is required, which translates in an additional power consumption, negating partially the low
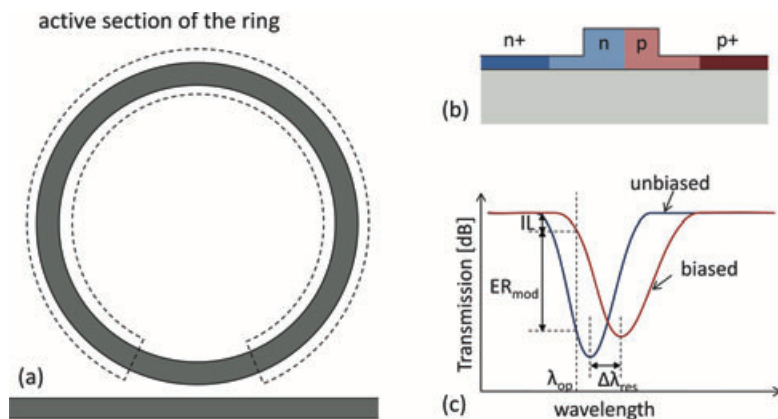

Figure 28 (online color at: www.lpr-journal.org) Schematic of a ring modulator. (a) Top view: the ring has an active section, where a (b) diode is embedded in the cross section. (c) When biased, the transmission drops: The modulator is operated on the slope of the ring.

energy consumption of the ring modulator. In addition to the spectral alignment requirements, the phase response of the modulated ring resonator can induce chirp in the signal if the signal bandwidth occupies a significant fraction of the ring linewidth.

4.4.2. Hybrid silicon rings

Instead of incorporating an active silicon section in the ring resonator, it is also possible to heterogeneously integrate other materials in the ring cavity, especially when those materials can introduce gain. The most obvious materials for that purpose are III-V semiconductors [10, 11, 181], which are widely used for semiconductor laser diodes.

Integrating III-V material on silicon is generally done by bonding techniques, either using direct bonding [11, 182] or using an adhesive material [12, 181, 183]. A thin film of III-V material is brought in close proximity to a silicon waveguide, enabling evanescent coupling, and when pumping the III-V material, optical gain. When incorporating such a gain medium in a ring, a laser cavity is formed [142]. However, the transition between silicon and the gain section can introduce losses (which should be overcome by the gain section) and reflections (which can generate additional counterdirectional coupling). When a ring is sufficiently large, there can be multiple resonances within the gain bandwidth of the III-V material. The evenly spaced peaks (which require some dispersion engineering, see Sect. 3.7) can be used to create a mode-locked laser [142]. Alternatively, one can integrate an active region over the entire ring, using optical pumping to generate gain [143, 184]

The same type of integration can be used to make an integrated III-V photodetector [13]. As the detector is embedded in the ring resonator, it will only respond to the ring resonant frequencies [143, 184, 185]. However, the loss introduced by the detector should be sufficiently small not to quench the ring resonance too much.

Alternatively, it is possible to implement the ring entirely in the III-V material: The silicon bus waveguide is now vertically coupled to the cavity. This eliminates the additional source of loss in the ring, and also enables a much stronger overlap of the optical mode with the gain medium. Most implementations of this principle rely on III-V disks rather than rings, as this facilitates the electrical contacting [12, 143, 186, 187].

5. Summary

In this paper, we have tried to give a comprehensive overview of the already prolific field of silicon microring resonators. The high confinement of silicon has made it possible to make resonators with an extremely small bend radius, footprint and a wide FSR. Especially this last property made it possible to build new functionality in silicon rings which was hitherto not possible in other materials. Over the past decade, the advances in silicon photonics have made these rings suitable for a variety of purposes,

from filters over sensors to the use in active devices such as modulators and lasers.

However, as we have discussed, not all aspects of silicon ring resonators are perfectly understood, and the high refractive index contrast of the silicon/oxide/air material system makes the silicon waveguides (and hence the rings) vulnerable to all kinds of imperfections, which in ring resonators translates into a variation in resonance wavelength, quality factor, counterdirectional coupling and resonance splitting.

The field of silicon ring resonators is very much alive, and better understanding a technological advances will definitely give us many exciting results in the coming decade, both in new physics as in valuable applications.

Wim Bogaerts is professor in the Photonics Research Group at Ghent University. He completed his studies in engineering (applied physics) at Ghent University in 1998 and joined the department of information technology (INTEC) at both Ghent University and the Interuniversity Microelectronics Center (IMEC) where he received his Ph. D. degree in 2004. In the photonics research group he specialized in the modeling, design and fabrication of nanophotonic components. Currently he coordinates the development of nanophotonic components in SOI in IMEC.

Peter De Heyn received the masters degree in photonics engineering from Ghent University and Vrije Universiteit Brussel (VUB), Belgium, in 2009. He is now working towards a Ph. D. degree in the Photonics Research Group of Ghent Unversity-IMEC, Belgium. He is working towards the heterogeneous integration of an ultra-dense wavelength demultiplexer including topics as narrow linewidth ring filters and

photo-detectors. Part of his work is supported by the FP7-BOOM project of the European Union.

Thomas Van Vaerenbergh received the masters degree in applied physics from Ghent University, Belgium, in 2010. Currently he works on a Ph. D. in the Photonics Research Group of IMEC-Ghent University.

Katrien De Vos received the masters degree in electrical engineering from Ghent University, Belgium, in 2005. Until 2010 she worked on a Ph. D. in the Photonics Research Group of IMEC-Ghent University. Her research topics included resonator-based label-free biosensors, passive SOI resonators and biocompatible integration with microfluidics. She attained her Ph. D. in 2010 and is now active as a product manager in the pharmaceutical industry.

Shankar Kumar Selvaraja received the M. Tech. degree in Optical communication from College of engineering, Anna University, Chennai, India, in 2004 and the M. Sc. degree in Microsystems and Microelectronics from University of Twente, The Netherlands, in 2005. In 2006 he joined the Photonics Research Group of Ghent University-imec, where he obtained a Ph. D. in 2011 on CMOS compatible process development for Photonic integrated circuits.

Tom Claes is currently researching silicon-on-insulator transducers for label-free biosensing towards obtaining a Ph. D. degree at the Photonics Research Group at the Department of Information Technology at Ghent University - IMEC, Belgium where he also obtained the master degree in electrical engineering in 2007.

Pieter Dumon received the degree in electrical engineering from Ghent University, Belgium, in 2002, where he received a Ph. D. degree in electrical engineering in 2007 for his work in wavelength filters in silicon photonic wires. He currently coordinates ePIXfab, a initiative for multi-project wafer fabrication in photonics.

Peter Bienstman received the Degree in electrical engineering and the Ph. D. degree from Ghent University, Belgium, in 1997 and 2001, respectively. He is currently an Associate Professor with the Department of Information Technology (INTEC), Ghent University. During 2001/2002, he was with the Joannopoulos Research Group, Massachusetts Institute of Technology (MIT). His research interests include several applications of nanophotonics (biosensors and photonic information processing), as well as nanophotonics modeling.

Dries Van Thourhout received the degree in physical engineering and the Ph. D. degree from Ghent University, Belgium in 1995 and 2000, respectively. From 2000 to 2002, he was with Lucent Technologies, Bell Laboratories, Crawford Hill, working on InPInGaAsP monolithically integrated devices. In 2002, he joined the Department of Information Technology (INTEC), Ghent University, continuing his work on integrated optoelectronic devices. Main interests are heterogeneous integration by wafer bonding, intrachip optical interconnect and WDM-devices.

Roel Baets is professor at Ghent University. He received MSc degrees in Electrical Engineering from Ghent University in 1980 and from Stanford University in 1981. He received a Ph. D. from Ghent University in 1984. From 1984 till 1989 he held a postdoctoral position at IMEC. Since 1989 he is professor in the Engineering Faculty in Ghent where he founded the Photonics Research Group. From 1990 till 1994 he has been part-time professor at the Technical University of Delft and from 2004 till 2008 at the Technical University of Eindhoven. Roel Baets has mainly worked in the field of integrated photonic components. He is also director of the multidisciplinary Center for Nano- and Biophotonics in Ghent.

References

[1] W. Bogaerts, R. Baets, P. Dumon, V. Wiaux, S. Beckx, D. Taillaert, B. Luyssaert, J. Van Campenhout, P. Bienstman, and D. Van Thourhout, J. Lightwave Technol. **23**(1), 401–412 (2005).

[2] W. M. J. Green, M. Rooks, L. Sekaric, and Y. Vlasov, Opt. Express **15**(25), 17106–17113 (2007).

[3] J. Fedeli, E. Augendre, J. Hartmann, L. Vivien, P. Grosse, V. Mazzocchi, W. Bogaerts, D. Van Thourhout, and F. Schrank, Photonics and electronics integration in the helios project, in: Proceedings of the 7th IEEE International Conference on Group IV Photonics (GFP), Beijing, China, 2010, pp. 356–358.

[4] C. Gunn, IEEE Micro **26**(2), 58–66 (2006).

[5] C. Gunn, Photonics Spectra **40**(3), 62–68 (2006).

[6] W. Bogaerts, P. Dumon, D. Van Thourhout, D. Taillaert, P. Jaenen, J. Wouters, S. Beckx, V. Wiaux, and R. Baets, J. Sel. Top. Quantum Electron. **12**(6), 1394–1401 (2006).

[7] W. Bogaerts, S. Selvaraja, P. Dumon, J. Brouckaert, K. De Vos, D. Van Thourhout, and R. Baets, J. Sel. Top. Quantum Electron. **16**(1), 33–44 (2010).

[8] D. Marris-Morini, L. Vivien, J. M. Fédéli, E. Cassan, P. Lyan, and S. Laval, Opt. Express **16**(1), 334–339 (2008).

[9] D. Marris-Morini, X. Le Roux, L. Vivien, E. Cassan, D. Pascal, M. Halbwax, S. Maine, S. Laval, J. M. Fédéli, and J. F. Damlencourt, Opt. Express **14**(22), 10838–10843 (2006).

[10] G. Roelkens, L. Liu, D. Liang, R. Jones, A. Fang, B. Koch, and J. Bowers, Laser Photon. Rev. **4**(6), 751–779 (2010).

[11] A. Fang, H. Park, O. Cohen, R. Jones, M. Paniccia, and J. Bowers, Opt. Express **14**(20), 9203–9210 (2006).

[12] J. Van Campenhout, P. Rojo Romeo, P. Regreny, C. Seassal, D. Van Thourhout, S. Verstruyft, L. Di Ciocco, J. M. Fedeli, C. Lagahe, and R. Baets, Opt. Express **15**(11), 6744–6749 (2007).

[13] J. Brouckaert, G. Roelkens, D. Van Thourhout, and R. Baets, IEEE Photon. Techol. Lett. **19**(19), 1484–1486 (2007).

[14] J. Heebner, R. Grover, and T. Ibrahim, Optical Microresonators: Theory, Fabrication and Applications, 1st edn., Springer Series in Optical Sciences (Springer, London, 2008).

[15] O. Schwelb, J. Lightwave Technol. **22**(5), 1380–1394 (2004).

[16] J. Heebner, V. Wong, A. Schweinsberg, R. Boyd, and D. Jackson, IEEE J. Quantum Electron. **40**(6), 726–730 (2004).

[17] B. E. Little, S. T. Chu, H. A. Haus, J. Foresi, and J. P. Laine, J. Lightwave Technol. **15**(6), 998–1005 (1997).

[18] C. Manolatou, M. J. Khan, S. H. Fan, P. R. Villeneuve, H. A. Haus, and J. D. Joannopoulos, IEEE J. Quantum Electron. **35**(9), 1322–1331 (1999).

[19] S. Selvaraja, P. Jaenen, W. Bogaerts, D. Van Thourhout, P. Dumon, and R. Baets, J. Lightwave Technol. **27**(18), 4076–4083 (2009).

[20] W. Bogaerts and S. Selvaraja, IEEE Photonics J. **3**(3), 422–432 (2011).

[21] A. Densmore, D. X. Xu, P. Waldron, S. Janz, P. Cheben, J. Lapointe, A. Delage, B. Lamontagne, J. H. Schmid, and E. Post, IEEE Photon. Technol. Lett. **18**(21–24), 2520–2522 (2006).

[22] K. Tiefenthaler and W. Lukosz, J. Opt. Soc. Am. B **6**(2), 209–220 (1989).

[23] G. J. Veldhuis, O. Parriaux, H. Hoekstra, and P. V. Lambeck, J. Lightwave Technol. **18**(5), 677–682 (2000).

[24] M. Popovic, C. Manolatou, and M. Watts, Opt. Express **14**(3), 1208–1222 (2006).

[25] T. J. Kippenberg, S. M. Spillane, and K. J. Vahala, Opt. Lett. **27**(19), 1669–71 (2002).

[26] J. Čtyroký, I. Richter, and V. Šinor, Optic. Quantum Electron. **38**(9–11), 781–797 (2010).

[27] B. E. Little, J. P. Laine, and S. T. Chu, Opt. Lett. **22**(1), 4–6 (1997).

[28] M. Borselli, T. Johnson, and O. Painter, Opt. Express **13**(5), 1515–30 (2005).

[29] F. Morichetti, Phys. Rev. Lett. **104**(3), 1–4 (2010).

[30] F. Morichetti, A. Canciamilla, M. Martinelli, A. Samarelli, R. De La Rue, M. Sorel, and A. Melloni, Appl. Phys. Lett. **96**(8), 081112 (2010).

[31] P. De Heyn, B. Kuyken, D. Vermeulen, W. Bogaerts, and D. Van Thourhout, in: Proceedings of the Optical Fiber Communication Conference and Exposition (OFC) and the National Fiber Optic Engineers Conference (NFOEC), Los Angeles, California, 2011, paper OThV.

[32] F. Morichetti, A. Canciamilla, and A. Melloni, Opt. Lett. **35**(11), 1777–1779 (2010).

[33] T. Wang, Z. Zhang, F. Liu, Y. Tong, J. Wang, Y. Tian, M. Qiu, and Y. Su, Opt. Comm. **282**(17), 3464–3467 (2009).

[34] Q. Li, Z. Zhang, J. Wang, M. Qiu, and Y. Su, Opt. Express **17**(2), 933–40 (2009).

[35] Q. Li, Z. Zhang, F. Liu, M. Qiu, and Y. Su, Appl. Phys. Lett. **93**(8), 081113 (2008).

[36] S. J. McNab, N. Moll, and Y. A. Vlasov, Opt. Express **11**(22), 2927–2939 (2003).

[37] Y. Vlasov and S. McNab, Opt. Express **12**(8), 1622–1631 (2004).

[38] T. Barwicz, M. A. Popovic, F. Gan, M. S. Dahlem, C. W. Holzwarth, P. T. Rakich, E. P. Ippen, F. X. Kartner, and H. I. Smith, Proc. SPIE **6872**, 68720Z-1–12 (2008).

[39] T. Tsuchizawa, K. Yamada, H. Fukuda, T. Watanabe, J. Takahashi, M. Takahashi, T. Shoji, E. Tamechika, S. Itabashi, and H. Morita, IEEE J. Sel. Top. Quantum Electron. **11**(1), 232–240 (2005).

[40] M. Notomi, A. Shinya, S. Mitsugi, E. Kuramochi, and H. Ryu, Opt. Express **12**(8), 1551–1561 (2004).

[41] M. Gnan, S. Thoms, D. Macintyre, R. De La Rue, and M. Sorel, Electron. Lett. **44**(2), 115–116 (2008).

[42] S. Selvaraja, Wafer-scale Fabrication Technology for Silicon Photonic Integrated Circuit, PhD Thesis, Ghent University, Belgium (2011).

[43] P. Dumon, Ultra-Compact Integrated Optical Filters in Silicon-on-insulator by Means of Wafer-Scale Technology, PhD Thesis, Ghent University, Belgium (2007).

[44] K. Lee, D. Lim, H. Luan, A. Agarwal, J. Foresi, and L. Kimerling, Appl. Phys. Lett. **77**(11), 1617–1619 (2000).

[45] S. Johnson, M. Povinelli, M. Soljacic, A. Karalis, S. Jacobs, and J. Joannopoulos, Appl. Phys. B **81**(2–3), 283–293 (2005).

[46] W. Bogaerts, P. Bienstman, and R. Baets, Opt. Lett. **28**(9), 689–691 (2003).

[47] J. H. Schmid, A. Delâge, B. Lamontagne, J. Lapointe, S. Janz, P. Cheben, A. Densmore, P. Waldron, D. X. Xu, and K. P. Yap, Opt. Lett. **33**(13), 1479–81 (2008).

[48] T. Barwicz and H. Haus, J. Lightwave Technol. **23**(9), 2719–2732 (2005).

[49] D. Sparacin, S. J. Spector, and L. C. Kimerling, J. Lightwave Technol. **23**(8), 2455 (2005).

[50] C. Y. Chao and L. J. Guo, Appl. Phys. Lett. **84**(14), 2479 (2004).

[51] T. Liang, L. Nunes, T. Sakamoto, K. Sasagawa, T. Kawanishi, M. Tsuchiya, G. Priem, D. Van Thourhout, P. Dumon, R. Baets, and H. Tsang, Opt. Express **13**(19), 7298–7303 (2005).

[52] D. Moss, L. Fu, I. Littler, and B. Eggleton, Electron Lett. **41**(6), 320–321 (2005).

[53] W. Bogaerts, V. Wiaux, D. Taillaert, S. Beckx, B. Luyssaert, P. Bienstman, and R. Baets, IEEE J. Sel. Top. Quantum Electron. **8**(4), 928–934 (2002).

[54] S. Selvaraja, W. Bogaerts, and D. Van Thourhout, Opt. Comm. **284**(8), 2141–2144 (2011).

[55] S. K. Selvaraja, K. De Vos, W. Bogaerts, P. Bienstman, D. Van Thourhout, and R. Baets, in: 2009 IEEE LEOS Annual Meeting Conference Proceedings, Vols. 1 and 2 (IEEE, New York, 2009), pp. 311–312.

[56] E. Dulkeith, F. Xia, L. Schares, W. Green, and Y. Vlasov, Opt. Express **14**(9), 3853–3863 (2006).

[57] A. C. Turner, C. Manolatou, B. S. Schmidt, M. Lipson, M. A. Foster, J. E. Sharping, and A. L. Gaeta, Opt. Express **14**(10), 4357–4362 (2006).

[58] P. Trinh, S. Yegnanarayanan, and B. Jalali, Electron. Lett. **31**(24), 2097–2098 (1995).

[59] P. Dumon, W. Bogaerts, V. Wiaux, J. Wouters, S. Beckx, J. Van Campenhout, D. Taillaert, B. Luyssaert, P. Bienstman, D. Van Thourhout, and R. Baets, IEEE Photon. Technol. Lett. **16**(5), 1328–1330 (2004).

[60] I. Christiaens, Vertically Coupled Microring Resonators Fabricated with Wafer Bonding, PhD Thesis, Ghent University, Belgium (2005).

[61] D. X. Xu, A. Densmore, P. Waldron, J. Lapointe, E. Post, A. Delâge, S. Janz, P. Cheben, J. H. Schmid, and B. Lamontagne, Opt. Express **15**(6), 3149–3155 (2007).

[62] C. Madsen and J. Zhao, Optical Filter design and Analysis, Wiley Series in Microwave and Optical Engineering (John Wiley & Sons, Inc., New York, 1999).

[63] Q. Wang, G. Farrell, and T. Freir, Opt. Comm. **259**(1), 133–136 (2006).

[64] M. Popovic, Theory and Design of High-Index-Contrast Microphotonic Circuits, PhD Thesis, MIT (2008).

[65] K. De Vos, Label-Free Silicon Photonics Biosensor Platform with Microring Resonators, PhD Thesis, Ghent University, Belgium (2010).

[66] M. Soltani, S. Yegnanarayanan, Q. Li, and A. Adibi, IEEE J. Sel. Top. Quantum Electron. **46**(8), 1158–1169 (2010).

[67] F. Xia, L. Sekaric, and Y. Vlasov, Opt. Express **14**(9), 3872–3886 (2006).

[68] W. R. McKinnon, D. X. Xu, C. Storey, E. Post, A. Densmore, A. Delage, P. Waldron, J. H. Schmid, and S. Janz, Opt. Express **17**(21), 18971–18982 (2009).

[69] S. K. Selvaraja, W. Bogaerts, P. Dumon, D. Van Thourhout, and R. Baets, J. Sel. Top. Quantum Electron. **16**(1), 316–324 (2010).

[70] R. Boeck, N. Jaeger, N. Rouger, and L. Chrostowski, Opt. Express **18**(24), 25151–25157 (2010).

[71] L. Jin, M. Li, and J. J. He, Opt. Comm. **284**(1), 156–159 (2011).

[72] L. Tobing, D. Lim., P. Dumon, R. Baets, and M. K. Chin, Appl. Phys. Lett. **92**(October), 101122 (2008).

[73] S. Darmawan, L. Tobing, P. Dumon, R. Baets, and M. K. Chin, IEEE Photon. Technol. Lett. **20**(18), 1560–1562 (2008).

[74] S. Darmawan, L. Tobing, P. Dumon, R. Baets, and M. K. Chin, IEEE Photon. Technol. Lett. **20**(1), 9–11 (2008).

[75] W. Bogaerts, P. Bradt, L. Vanholme, P. Bienstman, and R. Baets, Opt. Quantum Electron. **40**(11–12), 801–811 (2008), 17th International Workshop on Optical Waveguide Theory and Numerical Modelling, Eindhoven, Netherlands, JUN 13–14, 2008.

[76] Q. Li, M. Soltani, S. Yegnanarayanan, and A. Adibi, Opt. Express **17**(4), 2247–2254 (2009).

[77] Q. Li, M. Soltani, M. Atabaki, S. Yegnanarayanan, and A. Adibi, Opt. Express **17**(26), 23474–23487 (2009).

[78] J. Heebner, R. W. Boyd, and Q. H. Park, J. Opt. Soc. Am. B **19**(4), 722–731 (2002).

[79] S. Y. Cho and R. Soref, Opt. Express **16**(23), 19078–19090 (2008).

[80] F. Xia, L. Sekaric, and Y. Vlasov, Nature Photonics **1**(1), 65–71 (2007).

[81] K. O. Abrokwah, P. R. Chidambaram, and D. S. Boning, IEEE Transactions on Semiconductor Manufacturing **20**(2), 77–86 (2007).

[82] C. Hedlund, H. O. Blom, and S. Berg, J. Vac. Sci. Technol. A **12**(4), 1962–1965 (1994).

[83] M. Geng, L. Jia, L. Zhang, L. Yang, P. Chen, T. Wang, and Y. Liu, Opt. Express **17**(7), 5502–5516 (2009).

[84] P. Dong, W. Qian, H. Liang, R. Shafiiha, D. Feng, G. Li, J. Cunningham, A. Krishnamoorthy, and M. Asghari, Opt. Express **18**(19), 20298–20304 (2010).

[85] A. H. Atabaki, E. Shah Hosseini, A. A. Eftekhar, S. Yegnanarayanan, and A. Adibi, Opt. Express **18**(17), 18312–18323 (2010).

[86] D. Dai, L. Yang, and S. He, J. Lightwave Technol. **26**(5–8), 704–709 (2008).

[87] F. Gan, T. Barwicz, M. A. Popovic, M. S. Dahlem, C. W. Holzwarth, P. T. Rakich, H. I. Smith, E. P. Ippen, and F. X. Kartner, 2007 Photonics in Switching pp. 67–68 (2007).

[88] I. Kiyat, A. Aydinli, and N. Dagli, IEEE Photon. Technol. Lett. **18**(1–4), 364–366 (2006).

[89] J. Van Campenhout, W. Green, S. Assefa, and Y. Vlasov, Opt. Express **17**(26), 24020–24029 (2009).

[90] S. M. Lee, D. G. Cahill, and T. H. Allen, Phys. Rev. B **52**(1), 253 (1995).

[91] T. Coquil, E. K. Richman, N. J. Hutchinson, S. H. Tolbert, and L. Pilon, J. Appl. Phys. **106**(3), 034910–11 (2009).

[92] M. R. Watts, W. A. Zortman, D. C. Trotter, G. N. Nielson, D. L. Luck, and R. W. Young, 2009 Conference on Lasers and Electro-Optics and Quantum Electronics and Laser Science Conference (Cleo/Qels 2009), Vols 1–5 pp. 812–813 (2009).

[93] J. Cunningham, I. Shubin, X. Zheng, T. Pinguet, A. Mekis, Y. Luo, H. Thacker, G. Li, J. Yao, K. Raj, and A. V. Krishnamoorthy, Opt. Express **18**(18), 19055–19063 (2010).

[94] D. Sparacin, C. Y. Hong, L. C. Kimerling, J. Michel, J. P. Lock, and K. K. Gleason, Opt. Lett. **30**(17), 2251–2253 (2005).

[95] J. Schrauwen, D. Van Thourhout, and R. Baets, Opt. Express **16**(6), 3738–3743 (2008).

[96] J. Teng, P. Dumon, W. Bogaerts, H. Zhang, X. Jian, X. Han, M. Zhao, G. Morthier, and R. Baets, Opt. Express **17**(17), 14627–14633 (2009).

[97] D. Dimitropoulos, R. Claps, Y. Han, and B. Jalali, in: Proceedings of the Conference on Integrated Optics – Devices, Materials and Technologies VII, Netherlands, CA, 2003, edited by Y. S. Sidorin and A. Tervonen, Proc. SPIE, Vol. 4987 (2003), pp. 140–148.

[98] K. Tsia and B. Jalali, in: Proceedings of the Conference on Silicon Photonics and Photonic Integrated Circuits II, Brussels, Belgium, 2010, edited by G. C. Righini, Proc. SPIE, Vol. 7719 (2010).

[99] H. K. Tsang and Y. Liu, Semicon. Sci. Technol. **23**(6) (2008).

[100] M. Dinu, F. Quochi, and H. Garcia, Appl. Phys. Lett. **82**(18), 2954–2956 (2003).

[101] B. Jalali, R. Claps, D. Dimitropoulos, and V. Raghunathan, in: Silicon Photonics, Topics in Applied Physics, Vol. 94 (Springer, Berlin, Heidelberg, 2004), pp. 199–238.

[102] R. Claps, V. Raghunathan, D. Dimitropoulos, and B. Jalali, Opt. Express **11**(22), 2862–2872 (2003).

[103] R. Claps, D. Dimitropoulos, and B. Jalali, Electron Lett. **38**(22), 1352–1354 (2002).

[104] A. Liu, H. Rong, and M. Paniccia, Opt. Express **12**(18), 4261–4268 (2004).

[105] T. Liang and H. Tsang, Appl. Phys. Lett. **85**(16), 3343–3345 (2004).

[106] R. Jones, H. Rong, A. Liu, A. Fang, M. Paniccia, D. Hak, and O. Cohen, Opt. Express **13**(2), 519–525 (2005).

[107] R. Claps, D. Dimitropoulos, V. Raghunathan, Y. Han, and B. Jalali, Opt. Express **11**(15), 1731–1739 (2003).

[108] H. Rong, A. Liu, R. Jones, O. Cohen, D. Hak, R. Nicolaescu, A. Fang, and M. Paniccia, Nature **433**(7023), 292–294 (2005).

[109] O. Boyraz and B. Jalali, Opt. Express **13**(3), 796–800 (2005).

[110] O. Boyraz and B. Jalali, Opt. Express **12**(21), 5269–5273 (2004).

[111] E. Dulkeith, A. VlasovYu., X. Chen, N. Panoiu, and R. Osgood, Opt. Express **14**(12), 5524–5534 (2006).

[112] R. Dekker, A. Driessen, T. Wahlbrink, C. Moormann, J. Niehusmann, and M. Foerst, Opt. Express **14**(18), 8336–8346 (2006).

[113] R. Soref and B. Bennett, J. Quantum Electron. **23**(1), 123–129 (1987).

[114] H. Tsang, C. Wong, T. Liang, I. Day, S. Roberts, A. Harpin, J. Drake, and M. Asghari, Appl. Phys. Lett. **80**(3), 416–418 (2002).

[115] P. Dumon, G. Priem, L. Nunes, W. Bogaerts, D. Van Thourhout, P. Bienstman, T. Liang, M. Tsuchiya, P. Jaenen, S. Beckx, J. Wouters, and R. Baets, Japanese J. Appl. Phys. part 1 **45**(8B), 6589–6602 (2006).

[116] R. Jacobsen, K. Andersen, P. Borel, J. Fage-Pedersen, L. Frandsen, O. Hansen, M. Kristensen, A. Lavrinenko, G. Moulin, H. Ou, C. Peucheret, B. Zsigri, and A. Bjarklev, Nature **441**(7090), 199–202 (2006).

[117] V. Almeida and M. Lipson, Opt. Lett. **29**(20), 2387–2389 (2004).

[118] G. Priem, P. Dumon, W. Bogaerts, D. Van Thourhout, G. Morthier, and R. Baets, Opt. Express **13**(23), 9623–9628 (2005).

[119] Q. Xu and M. Lipson, Opt. Lett. **31**(3), 341–343 (2006).

[120] T. Johnson, M. Borselli, and O. Painter, Opt. Express **14**(2), 817–831 (2006).

[121] B. Corcoran, C. Monat, C. Grillet, D. J. Moss, B. J. Eggleton, T. P. White, L. O'Faolain, and T. F. Krauss, Nature Photonics **3**(4), 206–210 (2009).

[122] H. Fukuda, K. Yamada, T. Shoji, M. Takahashi, T. Tsuchizawa, T. Watanabe, J. Takahashi, and S. Itabashi, Opt. Express **13**(12), 4629–4637 (2005).

[123] M. Foster, A. Turner, J. Sharping, B. Schmidt, M. Lipson, and A. Gaeta, Nature **441**(7096), 960–963 (2006).

[124] S. Preble, Q. Xu, and M. Lipson, Nature Photonics **1**(5), 293–296 (2007).

[125] A. Turner, M. Foster, A. Gaeta, and M. Lipson, Opt. Express **16**(7), 4881–4887 (2008).

[126] K. Yamada, T. Fukuda, T. Watanabe, T. Tsuchizawa, H. Shinojima, T. Tanabe, M. Takahashi, and S. Itabashi, in: Proceedings of the 3rd International Conference on Group IV Photonics, Ottawa, Canada, 2006, pp. 237–239.

[127] R. Espinola, J. Dadap, R. Osgood, S. McNab, and Y. Vlasov, Opt. Express **13**(11), 4341–4349 (2005).

[128] R. Salem, M. Foster, A. Turner, D. F. Geraghty, M. Lipson, and A. Gaeta, Nature Photonics **2**(1), 35–38 (2008).

[129] K. Yamada, T. Tsuchizawa, T. Watanabe, H. Fukuda, H. Shinojima, T. Tanabe, and S. Itabashi, in: Proceedings of the 19th Annual Meeting of the IEEE-Lasers-and-Electro-Optics-Society, Montreal, Canada, 2006, Vols 1 and 2, pp. 613–614.

[130] S. Clemmen, K. P. Huy, W. Bogaerts, R. G. Baets, P. Emplit, and S. Massar, Opt. Express **17**(19), 16558–16570 (2009).

[131] H. Takesue, K. I. Harada, H. Fukuda, T. Tsuchizawa, T. Watanabe, K. Yamada, Y. Tokura, and S. I. Itabashi, J. Nanosci. Nanotechnol. **10**(3, Sp. Iss. SI), 1814–1818 (2010).

[132] I. W. Hsieh, X. Chen, X. Liu, J. Dadap, N. Panoiu, C. Y. Chou, F. Xia, W. Green, Y. Vlasov, and J. R. Osgood, Opt. Express **15**(23), 15242–15249 (2007).

[133] A. Savchenkov, A. Matsko, V. Ilchenko, I. Solomatine, D. Seidel, and L. Maleki, Phys. Rev. Lett. **101**(9) (2008).

[134] M. Popovic, H. Haus, and M. Watts, in: Proceedings of the 2006 Optical Fiber Communication Conference/National Fiber Optic Engineers Conference, Anaheim, CA, Mar. 05–10, 2006, pp. 714–716.

[135] K. De Vos, I. Bartolozzi, D. Taillaert, W. Bogaerts, P. Bienstman, R. Baets, and E. Schacht, Proc. SPIE **6447**(January), 6447DK–1 (2007).

[136] D. Taillaert, W. Van Paepegem, J. Vlekken, and R. Baets, in: Proc. SPIE, Vol. 6619 (2007), p. 661914.

[137] N. Yebo, P. Lommens, Z. Hens, and R. Baets, Opt. Express **18**(11), 11859–11866 (2010).

[138] N. Yebo, D. Taillaert, J. Roels, D. Lahem, M. Debliquy, D. Van Thourhout, and R. Baets, IEEE Photon. Technol. Lett. **21**(14), 960–962 (2009).

[139] M. Watts, D. Trotter, R. Young, and A. Lentine, in: Proceedings of the 5th IEEE International Conference on Group IV Photonics, Sorrento, Italy, 2008, pp. 4–6.

[140] Q. Xu, S. Manipatruni, B. Schmidt, J. Shakya, and M. Lipson, Opt. Express **15**(2), 430–436 (2007).

[141] T. Ye and X. Cai, J. Lightwave Technol. **28**(11), 1615–1623 (2010).

[142] B. Koch, A. Fang, O. Cohen, and J. E. Bowers, Opt. Express **15**(18), 11225–11233 (2007).

[143] L. Liu, G. Roelkens, J. Van Campenhout, J. Brouckaert, D. Van Thourhout, and R. Baets, J. Nanosci. Nanotechnol. **10**(3, Sp. Iss. SI), 1461–1472 (2010).

[144] J. Brouckaert, W. Bogaerts, S. Selvaraja, P. Dumon, R. Baets, and D. Van Thourhout, IEEE Photon. Technol. Lett. **20**(4), 309–311 (2008).

[145] J. Brouckaert, W. Bogaerts, P. Dumon, D. Van Thourhout, and R. Baets, J. Lightwave Technol. **25**(5), 1269–1275 (2007).

[146] C. W. Holzwarth, T. Barwicz, M. A. Popovic, P. T. Rakich, E. P. Ippen, F. X. Kaertner, and H. I. Smith, J. Vac. Sci. Technol. B **24**(6, Sp. Iss. SI), 3244–3247 (2006).

[147] B. Lee, B. Small, K. Bergman, Q. Xu, and M. Lipson, Opt. Lett. **31**(18), 2701–2703 (2006).

[148] M. Watts, T. Barwicz, M. Popovic, L. Socci, P. Rakich, E. Ippen, H. Smith, and F. Kaertner, in: Proceedings of the Conference on Lasers and Electro-Optics (CLEO), Vols 1–3, Baltimore, MD, 2005, pp. 269–272.

[149] T. Barwicz, H. Byun, F. Gan, C. W. Holzwarth, M. A. Popovic, P. T. Rakich, M. R. Watts, E. P. Ippen, F. X. Kaertner, H. I. Smith, J. S. Orcutt, R. J. Ram, V. Stojanovic, O. O. Olubuyide, J. L. Hoyt, S. Spector, M. Geis, M. Grein, T. Lyszczarz, and J. U. Yoon, J. Opt. Networking **6**(1), 63–73 (2007).

[150] J. K. S. Poon, J. Scheuer, Y. Xu, and A. Yariv, J. Opt. Soc. Am. B, Opt. Phys. **21**(9), 1665–1673 (2004).

[151] A. Melloni, A. Canciamilla, C. Ferrari, F. Morichetti, L. O'Faolain, T. Krauss, R. De La Rue, A. Samarelli, and M. Sorel, IEEE Photonics J. **2**(2), 181–194 (2010).

[152] J. K. Poon, L. Zhu, G. DeRose, and A. Yariv, Opt. Lett. **31**(4), 456–458 (2006).

[153] L. Y. Mario and M. K. Chin, Opt. Express **16**(3), 1796–1807 (2008).

[154] J. Yang, N. K. Fontaine, Z. Pan, A. O. Karalar, S. S. Djordjevic, C. X. Yang, W. Chen, S. Chu, B. E. Little, and S. J. B. Yoo, IEEE Photon. Technol. Lett. **20**(9–12), 1030–1032 (2008).

[155] A. Melloni, F. Morichetti, C. Ferrari, and M. Martinelli, Opt. Lett. **33**(20), 2389–2391 (2008).

[156] F. Morichetti, A. Melloni, C. Ferrari, and M. Martinelli, Opt. Express **16**(12), 8395–8405 (2008).

[157] M. S. Rasras, C. K. Madsen, M. A. Cappuzzo, E. Chen, L. T. Gomez, E. J. Laskowski, A. Griffin, A. Wong-Foy, A. Gasparyan, A. Kasper, J. Le Grange, and S. S. Patel, IEEE Photon. Technol. Lett. **17**(4), 834–836 (2005).

[158] F. Morichetti, C. Ferrari, A. Canciamilla, and A. Melloni, Laser and Photonics Reviews (2011).

[159] X. Fan, I. White, S. Shopoua, H. Zhu, J. Suter, and Y. Sun, Analytica Chimica Acta **620**(1–2), 8–26 (2008).

[160] A. Qavi, A. Washburn, J. Y. Byeon, and R. Bailey, Analytical and Bioanalytical Chemistry **394**(1), 121–135 (2009).

[161] K. De Vos, J. Girones, S. Popelka, E. Schacht, R. Baets, and P. Bienstman, Biosens Bioelectron **24**(8), 2528–33 (2009).

[162] J. Voros, Biophys. J. **87**(1), 553–561 (2004).

[163] K. F. Palmer and D. Williams, J. Opt. Soc. Am. **64**(8), 1107–1110 (1974).

[164] I. White and X. Fan, Opt. Express **16**(2), 1020–1028 (2008).

[165] J. Hu, X. Sun, A. Agarwal, and L. Kimerling, J. Opt. Soc. Am. B **26**(5), 1032–1041 (2009).

[166] K. De Vos, J. Girones, T. Claes, Y. De Koninck, S. Popelka, E. Schacht, R. Baets, and P. Bienstman, IEEE Photonics J. **1**(4), 225–235 (2009).

[167] D. X. Xu, M. Vachon, A. Densmore, R. Ma, A. Delage, S. Janz, J. Lapointe, Y. Li, G. Lopinski, D. Zhang, Q. Y. Liu, P. Cheben, and J. H. Schmid, Opt. Lett. **35**(16), 2771–2773 (2010).

[168] M. Luchansky, A. Washburn, T. Martin, M. Iqbal, L. Gunn, and R. Bailey, Biosens. Bioelectron. **26**(4), 1283–1291 (2010).

[169] J. Homola, Chemical Reviews **108**(2), 462–493 (2008).

[170] D. X. Xu, M. Vachon, A. Densmore, R. Ma, S. Janz, A. Delage, J. Lapointe, P. Cheben, J. H. Schmid, E. Post, S. Messaoudene, and J. M. Fedeli, Opt. Express **18**(22), 22867–22879 (2010).

[171] M. Iqbal, M. Gleeson, B. Spaugh, F. Tybor, W. Gunn, M. Hochberg, T. Baehr-Jones, R. Bailey, and L. Gunn, J. Sel. Top. Quantum Electron. **16**(3), 654–661 (2010).

[172] A. Washburn, M. Luchansky, A. Bowman, and R. Bailey, Analy. Chem. **82**(1), 69–72 (2010).

[173] A. Qavi and R. Bailey, Ang. Chem. **49**(27), 4608–4611 (2010).

[174] G. T. Reed, G. Mashanovich, F. Y. Gardes, and D. J. Thomson, Nature Photonics **4**(8), 518–526 (2010).

[175] S. Manipatruni, Q. Xu, B. Schmidt, J. Shakya, and M. Lipson, in: Proceedings of the IEEE/LEOS 20th Annual Meeting, Lake Buena Vista, Florida, 2007, pp. 537–538.

[176] S. Manipatruni, Q. Xu, and M. Lipson, Opt. Express **15**(20), 13035–13042 (2007).

[177] L. Liao, A. Liu, J. Basak, H. Nguyen, M. Paniccia, D. Rubin, Y. Chetrit, R. Cohen, and N. Izhaky, Electron. Lett. **43**(22) (2007).

[178] F. Gardes, G. Reed, N. Emerson, and C. Png, Opt. Express **13**(22), 8845–8854 (2005).

[179] A. Liu, L. Liao, D. Rubin, H. Nguyen, B. Ciftcioglu, Y. Chetrit, N. Izhaky, and M. Paniccia, Opt. Express **15**(2), 660–668 (2007).

[180] P. Dong, S. Liao, D. Feng, H. Liang, D. Zheng, R. Shafiiha, C. C. Kung, W. Qian, G. Li, X. Zheng, A. Krishnamoorthy, and M. Asghari, Opt. Express **17**(25), 22484–22490 (2009).

[181] G. Roelkens, J. V. Campenhout, J. Brouckaert, D. V. Thourhout, R. Baets, P. R. Romeo, P. Regreny, A. Kazmierczak, C. Seassal, X. Letartre, G. Hollinger, J. Fedeli, L. D. Cioccio, and C. Lagahe-Blanchard, Materials Today **10**(7–8), 36–43 (2007).

[182] M. Kostrzewa, L. D. Cioccio, M. Zussy, J. Roussin, J. Fedeli, N. Kernevez, P. Regreny, C. Lagahe-Blanchard, and B. Aspar, Sens. Act. A, Phys. **125**(2), 411–414 (2006).

[183] G. Roelkens, D. Van Thourhout, and R. Baets, Electron. Lett. **41**(9), 561–562 (2005).

[184] G. Roelkens, L. Liu, D. Van Thourhout, R. Baets, R. Notzel, F. Raineri, I. Sagnes, G. Beaudoin, and R. Raj, J. Appl. Phys. **104**(3) (2008).

[185] D. Van Thourhout, T. Spuesens, S. Selvaraja, L. Liu, G. Roelkens, R. Kumar, G. Morthier, P. Rojo-Romeo, F. Mandorlo, P. Regreny, O. Raz, C. Kopp, and L. Grenouillet, J. Sel. Top. Quantum Electron. **16**(5), 1363–1375 (2010).

[186] P. R. Romeo, J. V. Campenhout, P. Regreny, A. Kazmierczak, C. Seassal, X. Letartre, G. Hollinger, D. V. Thourhout, R. Baets, J. M. Fedeli, and L. D. Cioccio, Opt. Express **14**(9), 3864–3871 (2006).

[187] J. Van Campenhout, L. Liu, P. Romeo, D. Van Thourhout, C. Seassal, P. Regreny, L. Di Cioccio, J. M. Fedeli, and R. Baets, IEEE Photon. Technol. Lett. **20**(16), 1345–1347 (2008).